AGU PUBLICATIONS

JGR

Journal of Geophysical Research: Solid Earth

RESEARCH ARTICLE
10.1002/2013JB010730

Key Points:
- Marine swath 3-D seismic imaging of the axial melt lens at the East Pacific Rise
- Quantification of the physical properties of the axial melt lens
- Constraints on the source and volume of the 2005–2006 seafloor eruption

Correspondence to:
J. P. Canales,
jcanales@whoi.edu

Citation:
Xu, M., J. Pablo Canales, S. M. Carbotte, H. Carton, M. R. Nedimović, and J. C. Mutter (2014), Variations in axial magma lens properties along the East Pacific Rise (9°30′N–10°00′N) from swath 3-D seismic imaging and 1-D waveform inversion, *J. Geophys. Res. Solid Earth*, *119*, 2721–2744, doi:10.1002/2013JB010730.

Received 27 SEP 2013
Accepted 5 APR 2014
Accepted article online 9 APR 2014
Published online 29 APR 2014

Variations in axial magma lens properties along the East Pacific Rise (9°30′N–10°00′N) from swath 3-D seismic imaging and 1-D waveform inversion

Min Xu[1,2], J. Pablo Canales[3], Suzanne M. Carbotte[4], Helene Carton[4], Mladen R. Nedimović[4,5], and John C. Mutter[4]

[1]Massachusetts Institute of Technology–Woods Hole Oceanographic Institution Joint Program, Woods Hole, Massachusetts, USA, [2]Now at GeoTomo LLC, Houston, Texas, USA, [3]Department of Marine Geology and Geophysics, Woods Hole Oceanographic Institution, Woods Hole, Massachusetts, USA, [4]Department of Marine Geology and Geophysics, Lamont-Doherty Earth Observatory, Palisades, New York, USA, [5]Department of Earth Sciences, Dalhousie University, Halifax, Nova Scotia, Canada

Abstract We use three-dimensional multistreamer seismic reflection data to investigate variations in axial magma lens (AML) physical properties along the East Pacific Rise between 9°30′N and 10°00′N. Using partial-offset stacks of *P*- and *S*-converted waves reflecting off the top of the AML, we image four 2–4 km long melt-rich sections spaced 5–10 km from each other. One-dimensional waveform inversion indicates that the AML in a melt-rich section is best modeled with a low *Vp* (2.95–3.23 km/s) and *Vs* (0.3–1.5 km/s), indicating >70% melt fraction. In contrast, the AML in a melt-poor section requires higher *Vp* (4.52–4.82 km/s) and *Vs* (2.0–3.0 km/s), which indicates <40% melt fraction. The thicknesses of the AML are constrained to be 8–32 m and 8–120 m at the melt-rich and -poor sites, respectively. Based on the AML melt-mush segmentation imaged in the area around the 2005–2006 eruption, we infer that the main source of this eruption was a 5 km long section of the AML between 9°48′N and 51′N. The eruption drained most of the melt in this section of the AML, leaving behind a large fraction of connected crystals. We estimate that during the 2005–2006 eruption, a total magma volume of $9–83 \times 10^6$ m^3 was extracted from the AML, with a maximum of 71×10^6 m^3 left unerupted in the crust as dikes. From this, we conclude that an eruption of similar dimensions to the 2005–2006, one would be needed with a frequency of years to decades in order to sustain the long-term average seafloor spreading rate at this location.

1. Introduction

The fast spreading East Pacific Rise (EPR) has been extensively studied during the last 3 decades following the discovery of a bright seismic reflection event beneath the ridge axis, which was interpreted to originate from the roof of an axial magma chamber (AMC) [*Herron et al.*, 1978]. The large number of multidisciplinary studies conducted at the EPR between ~9°N and 10°N led to the establishment of this region as a RIDGE2000 Integrated Study Site (R2K ISS) (http://www.ridge2000.org/). The presence of an AMC along most of this section of the EPR was established in the 1990s [e.g., *Detrick*, 1991; *Detrick et al.*, 1987; *Dunn and Toomey*, 1997; *Kent et al.*, 1990, 1993a, 1993b; *Mutter et al.*, 1988; *Vera et al.*, 1990]. The size and shape of this magma body have been the subject of several investigations [*Caress et al.*, 1992; *Collier and Singh*, 1997, 1998; *Detrick et al.*, 1993, 1987; *Harding et al.*, 1989; *Hussenoeder et al.*, 1996; *Kent et al.*, 1990, 1993a, 1993b; *Singh et al.*, 1998, 1999; *Toomey et al.*, 1990; *Vera et al.*, 1990]. These studies have led to a model in which a thin (<200 m) [e.g., *Hussenoeder et al.*, 1996], narrow (usually 1–2 km wide, with extreme values 0.25 km and 4.15 km [*Kent et al.*, 1993b]) lens or sill of magma 1–2 km below the seafloor [e.g., *Detrick et al.*, 1987] overlies a zone of partial melt in the midcrust surrounded by a broader low-velocity volume (5–10 km wide) extending to the base of the crust and into the uppermost mantle [*Dunn et al.*, 2000; *Sinton and Detrick*, 1992]. The thickness of the axial magma lens (AML), forming the roof of the AMC, has not been well constrained because of the lack of robust evidence for basal AML reflections in field data. Waveform modeling suggests that the AML is characterized by a decrease in seismic velocity across the boundary between an ~50 m thick solid layer separating the magma chamber from the upper crustal hydrothermal

fluids and a thin (~30–100 m) sill of melt and crystals [e.g., *Collier and Singh*, 1997, 1998; *Hussenoeder et al.*, 1996; *Singh et al.*, 1998, 1999]. In this paper we use the terms "melt lens" or "melt sill" indistinguishably to refer to the partially or fully molten AML capping the larger low-velocity, high-temperature zone of the lower crust [e.g., *Dunn et al.*, 2000].

Although the AML is volumetrically small, it is thought to play a key role in the availability and composition of magma at the ridge axis [*Sinton and Detrick*, 1992]. Understanding the nature and physical state of the AML at the EPR provides key constrains for seafloor eruption processes, the chemistry of the erupted lavas, and the accretion of oceanic crust. However, the internal properties (e.g., crystallinity and distribution of crystals) of the AML and their spatial and temporal variations along the northern EPR are poorly known. The shear properties of the AML are a proxy for its molten state, but can only be inferred from their effect on amplitude versus offset (AVO) behavior of reflected seismic phases, including *P*-to-*S*-converted phases. The shear wave velocity (*Vs*) within the AML has been estimated at a few locations along the EPR with variable results. On the basis of plane wave reflection coefficient modeling of an expanding spread profile at 13°13′N, *Harding et al.* [1989] inferred the presence of a partially molten AML (i.e., $Vs \neq 0$ km/s). In contrast, an AVO analysis of the AML event at 9°30′N led *Vera et al.* [1990] to suggest the presence of a fully molten sill (i.e., $Vs = 0$ km/s). In some instances, results from the same location obtained by different investigators using the same data are inconsistent with each other. For example, the estimates of AML *Vs* at EPR 9°39′N range from 0 km/s [*Collier and Singh*, 1997] to 1.45 km/s [*Hussenoeder et al.*, 1996]. Other than the waveform inversion investigation at the southern EPR (~14°S) [*Singh et al.*, 1998, 1999], none of these studies have used information from shear waves reflected from the AML, which provides better constraints on *Vs* structure of the lens.

A general conclusion extracted from these studies is that AML properties vary along the global mid-ocean ridge (MOR) system. The different AVO behavior of *P*- and *S*-converted waves reflecting off a partially molten sill, and the AVO dependence with melt content allowed *Singh et al.* [1998] to produce qualitative estimates of the spatial scale of along-axis variations in melt content within the AML inferred from *P* and *S* wave partial-offset stacks. This approach has been employed at the southern EPR [*Singh et al.*, 1998], southern Juan de Fuca Ridge (JdFR) [*Canales et al.*, 2006], and the EPR 9°03′N overlapping spreading center (OSC) [*Singh et al.*, 2006]. However, at the EPR R2K ISS, studies of the physical properties of the AML using either partial-offset stacking (except locally at the 9°03′N OSC but only for *P* waves [*Singh et al.*, 2006]) or waveform inversion using information from both AML-reflected *P* and *S* waves have not been attempted.

In summer 2008, we conducted a multistreamer, multichannel seismic (MCS) reflection experiment onboard the R/V *Marcus G. Langseth* across and along the northern EPR between the Siqueiros and Clipperton transform faults (cruise *MGL0812*) [*Mutter et al.*, 2009]. The primary goal of cruise *MGL0812* was to create an accurate 3-D seismic reflection image of the magmatic-hydrothermal systems within the EPR 9°50′N site by imaging the structure of the AML and shallow oceanic crust at a resolution, geometric accuracy, and scale comparable to the seafloor observations of hydrothermal, biological, and volcanic activities [*Mutter et al.*, 2009]. This new data set has resulted to date in the discovery of off-axis magmatic systems [*Canales et al.*, 2012; *Han et al.*, 2014], the recognition that fine-scale segmentation of the AML coincides with that of the seafloor eruptive fissure zone and limits the lateral magma mixing within the AML [*Carbotte et al.*, 2013], and that changes in 3-D Moho reflection character arise from variations in crustal accretion style and correlate with third-order axial segmentation [*Aghaei et al.*, 2014].

In this study we use this new data set to investigate the spatial variation in melt content and the physical properties of the AML along the northern EPR (~9°30′N–10°N) using *P* and *S* wave partial-offset stackings and 1-D waveform inversion methods. Our results show four prominent 2–4 km long melt-rich sections (>70% melt) spaced 5–10 km from each other, with the remaining AML sections having low-to-intermediate melt content (<40%). One of these melt-poor sections is spatially coincident with the center of the 2005–2006 eruption, allowing us to provide new constraints on some of the characteristics of this recent eruption.

2. Geological and Geophysical Backgrounds

The northern EPR is the boundary between the Pacific and Cocos tectonic plates (Figure 1a). The EPR 8°–11°N R2K ISS includes a long first-order ridge-axis segment bounded by the Clipperton transform fault to the north and the Siqueiros transform fault to the south. This segment is one of the best studied portions of the world's MOR system [e.g., *Fornari et al.*, 2012]. The full spreading rate in this area has been approximately 110 mm/yr

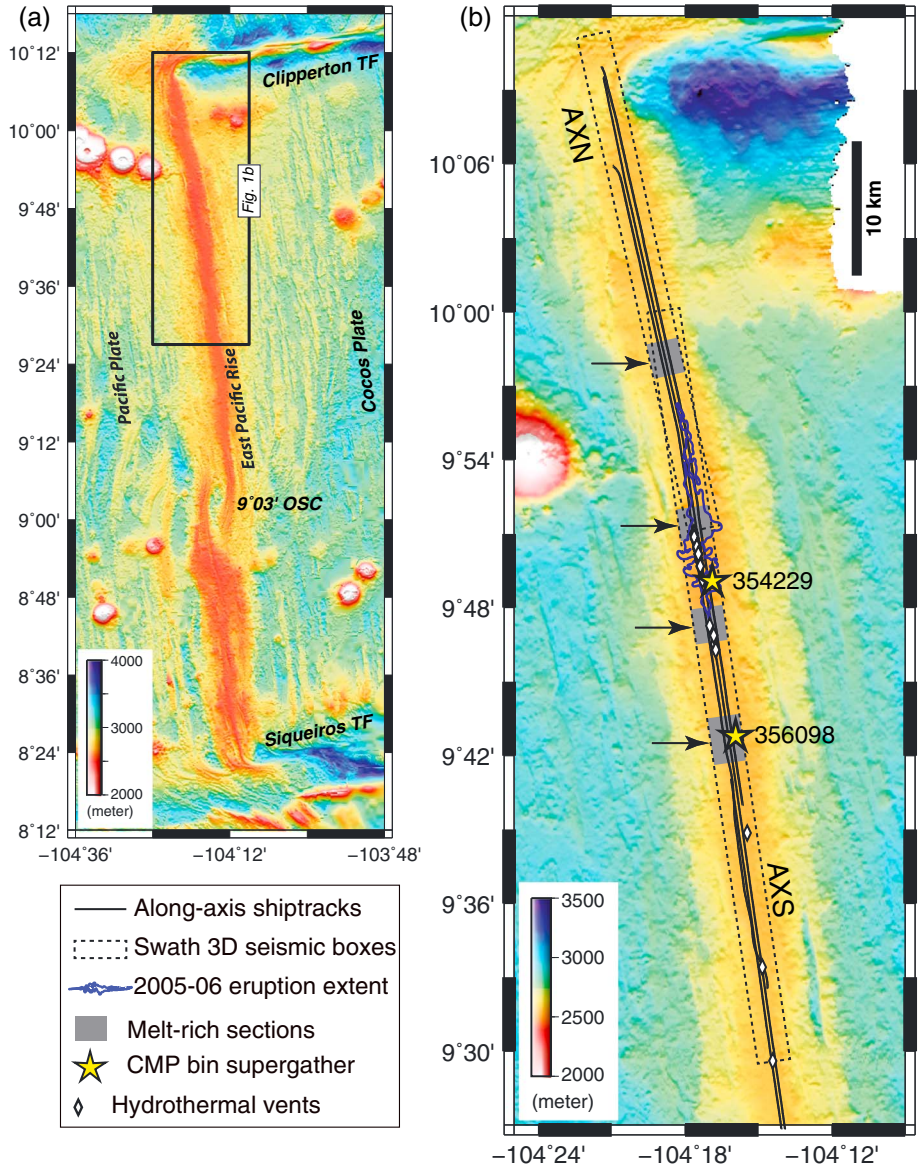

Figure 1. (a) Shaded bathymetric relief of the East Pacific Rise between Siqueiros and Clipperton fracture zones (EPR, 8°12′N–10°15′N). Bathymetry data are from the Global Multiresolution Topography synthesis [*Ryan et al.*, 2009] available from the Marine Geoscience Data System (http://www.marine-geo.org). (b) Bathymetry map of our study area (EPR, ~9°30′N–10°N). Data are from cruise *MGL0812* [*Mutter et al.*, 2009]. Two swath 3-D along-axis seismic boxes (dashed rectangles) were investigated using *P* and *S* wave partial-offset stacking: AXS (~9°30′N–10°N) and AXN (~9°51′N–10°10′N). Arrows point to melt-rich sections identified from our analysis (shaded rectangles): four prominent 2–4 km long melt-rich sections are found at ~9°42′N–9°44′N, 9°47′N–9°48′N, 9°51′N–9°52′N, and 9°57′N–9°58′N. Solid lines show the ship tracks of the four along-axis seismic lines used in this study. Blue line marks the extent of 2005–2006 eruption derived from camera tow data [*Soule et al.*, 2007]. White diamonds indicate hydrothermal vents. Yellow stars with numbers show the positions of the two CMP bin supergathers used for 1-D waveform modeling. The area of study shown in Figure 1b is outlined with a black box.

during the past 2 Myr [*Carbotte and Macdonald*, 1992]. The whole segment is believed to be magmatically active, as inferred from morphological observations [*Macdonald and Fox*, 1988; *Scheirer and Macdonald*, 1993], the along-axis continuity and seismic brightness of the AML [*Detrick et al.*, 1987; *Herron et al.*, 1980; *Kent et al.*, 1993b; *Mutter et al.*, 1988], the presence of crustal and upper mantle low seismic velocity and high-attenuation zones [*Dunn and Toomey*, 1997; *Dunn et al.*, 2000; *Toomey et al.*, 1994, 1990, 2007; *Wilcock et al.*, 1992, 1995], and the abundance of high-temperature hydrothermal activity [*Haymon et al.*, 1991].

Table 1. Summary of Seismic Data Acquisition Parameters for Cruise *MGL0812*

Acquisition Parameters	
Sources (air gun arrays)	Number of source arrays: 2 (each with 2 strings) Number of guns: 10 per array (1 spare) Source separation: 75 m Volume: 54 L (3300 in^3) per source Shot interval: alternate every 37.5 m Source depth: 7.5 m
Receivers (hydrophone streamers)	Number: 4 Spacing: 150 m Length: 6000 m Number of channels: 468 per streamer Channel spacing: 12.5 m Receiver depth: 7.5 m (AXIS3 and AXIS2R1) 10 m (AXIS4 and AXIS3P2)[a]
Source to nearest channel distance	200 m
Data recording	Sampling interval: 2 ms Record length: 8.190 s (AXIS3 and AXIS2R1) 10.240 s (AXIS4 and AXIS3P2)[a] Format: SEG-D

[a]For profiles AXIS4 and AXIS3P2: due to the weather conditions, the depth of the steamers were lowered from 7.5 to 10 m to help alleviate persistent cable swell noise.

Two second-order segments separated by the 9°03′N OSC (Figure 1a) and multiple-finer-scale segments, including third-order volcanic segments, which are defined by discontinuities in the structure and morphology of the axial topographic high and in the near-axis ridge flank fabric, and fourth-order segments bounded by smaller, more transient ridge axis discontinuities, are identified through multibeam and side-scan sonar imaging [e.g., *Haymon et al.*, 1991; *Macdonald and Sempéré*, 1984; *Scheirer and Macdonald*, 1993; *White et al.*, 2006, 2002]. The morphotectonic/structural segmentation of the ridge crest at the fourth-order scale matches remarkably well with the along-strike variability observed in axial hydrothermal activity, and the fourth-order segments appear to be in various stages of magmatic, tectonic, and hydrothermal developments [*Haymon et al.*, 1991].

The EPR 9°50′N area is the first MOR segment with multiple documented eruptions [e.g., *Haymon et al.*, 1993; *Soule et al.*, 2009, 2007; *Tolstoy et al.*, 2006]. The 2005–2006 eruption (Figure 1b) occurred in approximately the same area as an eruption documented in 1991–1992 [*Haymon et al.*, 1993; *Rubin et al.*, 1994; *Soule et al.*, 2007]. Using seafloor imagery collected on camera tows and *Alvin* dives, *Soule et al.* [2007] estimated that the 2005–2006 eruption produced ~22×10^6 m^3 of lava, 4–5 times larger than the estimated volumes of the 1991–1992 erupted lava flows.

Potential eruptions from melt, accumulated within an AML, depend on a number of parameters including the internal properties of the sill [*Singh et al.*, 1998], which have only been investigated so far in two locations at this EPR section. At 9°48′N, *Collier and Singh* [1997, 1998] concluded that the ridge is underlain by a thin (30 m) layer with low *Vp* (2.4 km/s) and *Vs* (~ 0 km/s). This layer was interpreted as a magma sill with less than 20 ± 10% crystals, underlain by mostly solid floor. The melt layer was inferred to have been newly emplaced, suggesting that this segment was at the onset of a renewed volcanic stage. At 9°39′N, *Collier and Singh* [1998] also inferred a high-melt content within the AML based on $Vs < 1$ km/s, but found that the base of the mostly molten layer was underlain by a velocity gradient interpreted as a downward increase in crystallinity from 20% to 40–90% over just 50 m, suggesting that this segment was at an intermediate stage in its volcanic cycle. However, at this same location and using the same data but a different methodology, *Hussenoeder et al.* [1996] inferred that the AML at 9°39′N is ~82 m thick with $Vp = 3.40$ km/s and $Vs = 1.45$ km/s, suggesting a lower melt content within the AML.

3. Seismic Data Acquisition and Processing

We use a subset of the *MGL0812* MCS data set consisting of along-axis swath 3-D MCS data collected along up to four closely spaced axis-parallel sail lines between ~9°30′N and 10°00′N (Figure 1b). Seismic data acquisition parameters for cruise *MGL0812* are listed in Table 1; more details of the data acquisition can be found in *MGL0812* cruise report [*Mutter et al.*, 2008]. Accurate locations of shots and hydrophone groups were

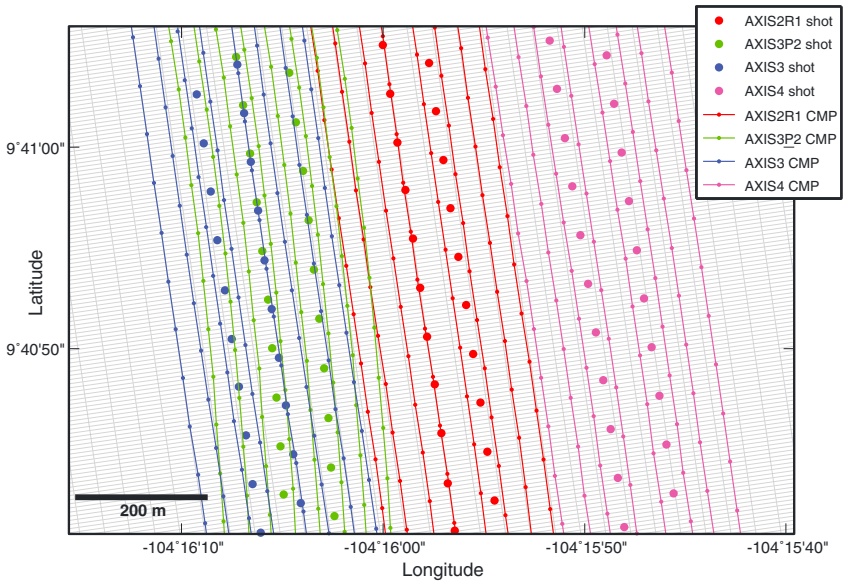

Figure 2. A zoom-in view of the experimental configuration of cruise *MGL0812* [*Mutter et al.*, 2009] for swath 3-D box AXS. The colored lines connect source-receiver midpoints (small solid circles) that correspond to common source and streamer pairs. Shot locations are indicated by large solid circles. Only 1 out of every 12 midpoints and 1 out of every 2 shots are shown for clarity purposes. A different color is used for each sail line. The background gray mesh shows the swath 3-D geometry setup with 37.5 m × 6.25 m CMP bins.

obtained from the ship's Global Positioning System (GPS), GPS receivers on the tail buoys at the end of the streamers, and acoustic transponders and compasses placed along the streamers. For each multisource, multistreamer sail line and assuming nominal geometry, the experiment configuration [*Mutter et al.*, 2009] resulted in eight common midpoint (CMP) seismic reflection profiles (i.e., in-lines, here oriented parallel to the ridge axis) separated 37.5 m from each other. For improved imaging, the data were binned in 3-D. For this, two overlapping swath 3-D along-axis boxes were created: the southern box AXS includes seismic data from sail lines AXIS2R1, AXIS3, AXIS4, and AXIS3P2 and the northern box AXN includes seismic data from sail lines AXIS2R1, AXIS4, and AXIS3P2 (Figure 1b). The two swath 3-D boxes were then divided into 37.5 m × 6.25 m CMP bins, and the data traces were sorted to corresponding CMP bins for processing (Figure 2).

The detailed seismic processing sequence and the parameters used are listed in Table 2. Seismic processing was designed to enhance stacking of the AML-reflected waves. It consisted of conventional steps [e.g., *Yilmaz*, 1987] such as trace editing, sorting to CMP bin gathers, band-pass filtering, spherical divergence and surface-consistent amplitude corrections, flexible binning (Figure 3), creating CMP bin supergathers, trace interpolation, normal moveout (NMO) corrections, frequency-wave number (*f-k*) filtering, stacking, and migration (Table 2). The *f-k* filter was designed to improve the signal-to-noise ratio of AML-reflected *P* and *S* waves for partial-offset stacking (Figures 4c and 4d) by filtering out seafloor and shallow crustal reflections and diffractions and side echoes from rough seafloor topography that contaminate AML reflections at far offsets.

4. *P* and *S* Wave Partial-Offset Stackings

Melt has a strong effect on the crustal shear velocity [*Anderson and Spetzler*, 1970; *Mavko*, 1980] and therefore on the AVO behavior of *P*- ($P_{AML}P$) and *S*-converted ($P_{AML}S$) waves reflected off a crustal melt lens (Figure 5). The detection of $P_{AML}S$ waves allowed *Singh et al.* [1998] and *Canales et al.* [2006] to build seismic reflection images of melt-rich and melt-poor sections of the AML along the southern EPR and JdFR using 2-D MCS data. However, due to streamer feathering, there is an inherent ambiguity in imaging melt-rich and melt-poor sections of an AML with 2-D MCS data using this approach. This is because the AML can be as narrow as just a few hundred meters, and apparent AVO variations could be due to the misalignment of sources and receivers with respect to the center of the AML [*Kent et al.*, 1993a, 1993b] and not necessarily due to true changes in AML physical properties. This problem, which is not an issue when dealing with true 3-D data, can be mitigated using swath 3-D analysis of feathered 2-D data [*Nedimović and West*, 2003]. In this section, we describe the

Table 2. Data Processing Sequence and Parameters

Sequence	Steps and Parameters
Trace editing	
Swath 3-D geometry definition	CMP gather, 40-fold bin (bin size: 6.25 m × 37.5 m in along-axis and cross-axis direction, respectively) angles of 3-D boxes: AXM NW 8.3323° AXN: NW 12.5056°
Band-pass filtering	5-7-200-225 Hz
Offset-dependent spherical divergence correction	input velocity source: esp05 [*Vera et al.*, 1990]
Surface-consistent amplitude correction for shot and channel	
Flexible binning	offset distribution regularization (cross-line direction): 0.5 × bin size for offsets ≤1662 m; 1.5 × bin size for offsets ≥4587 m (linear interpolation offsets in between those values) (Figure 3)
Resample	4 ms and 7 s long
Creating CMP supergathers (along subline direction)	band-pass filter 2-7-30-50 Hz combining 24 consecutive CMP gathers and median-stacking constant-offset traces
Trace interpolation	CMP supergather: regularized 468-fold trace gathers, offset range: 190–6027.5 m (with an interval of 12.5 m)
Frequency wave number (*f-k*) filtering	band-pass filter 2-7-30-50 Hz NMO (2.0 km/s) *f-k* dip filter (apparent dips exceeding 6.25 ms/trace) remove NMO (2.0 km/s)
P and *S* wave partial-offset stacking	mute (stretch amount 65%) near-offset *P* wave stack: NMO (2.6 km/s), 0–2 km midoffset *P* wave stack: NMO (2.6 km/s), 2–4 km midoffset *S* wave stack: NMO (2.4 km/s), 2–4 km
Post-stack time migration	band-pass filter 2-7-30-50 Hz top mute at the seafloor finite difference algorithm [*Lowenthal et al.*, 1976] (maximum dip 15 ms/trace, layer thickness 40 ms)
Display	band-pass filter 2-7-30-50 Hz energy attribute of trace segment: time window for *P* wave stack: 3.9–4.15 s time window for *S* wave stack: 4.15–4.4 s

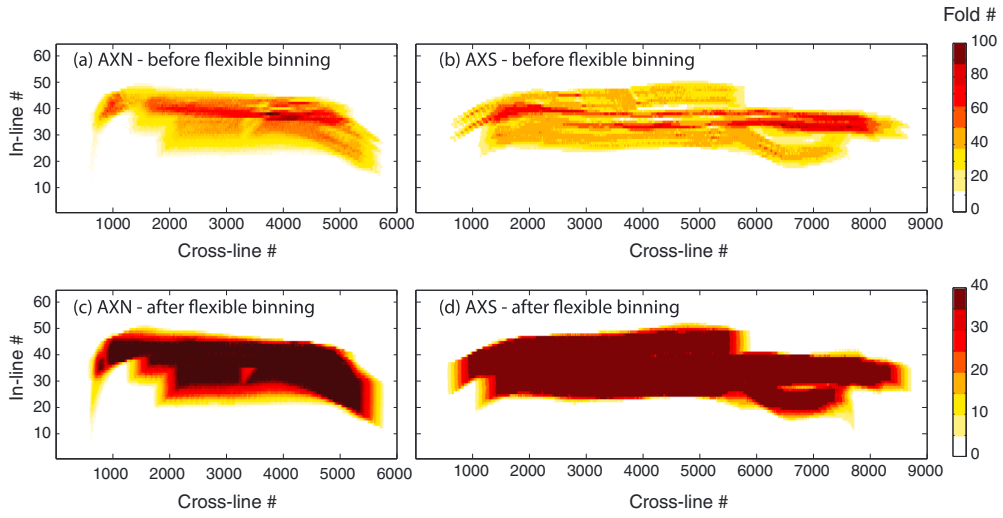

Figure 3. Bin fold map for 3-D seismic boxes AXN (a) before and (c) after flexible binning, and AXS (b) before and (d) after flexible binning. The flexible binning is based on offset distribution regularization (cross-line direction) using 0.5 × bin size for offsets ≤ 1662 m, 1.5 × bin size for offsets ≥ 4587 m (linear interpolation offsets in between those values). The nominal bin fold after flexible binning is 40.

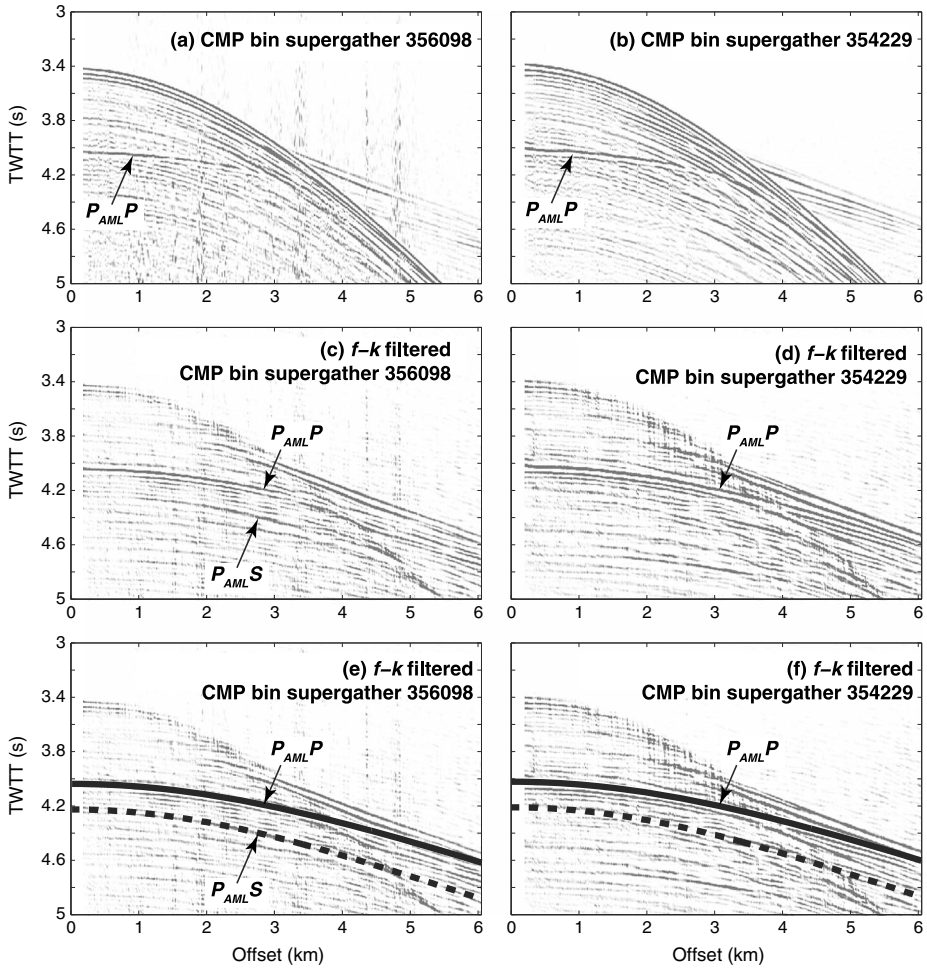

Figure 4. Two contrasting CMP bin supergathers from swath 3-D seismic box AXS. (a) CMP bin supergather 356098. (b) CMP bin supergather 354229. Their corresponding (c–f) frequency-wave number (*f-k*) filtered gathers are also shown. The AML reflections, $P_{AML}P$ and $P_{AML}S$, are indicated by black arrows. Figures 4e and 4f same as Figures 4c and 4d with predicted $P_{AML}P$ and $P_{AML}S$ travel time curves (solid and dashed black lines, respectively) calculated from velocity model ESP05 [*Vera et al.*, 1990]. TWTT is two-way travel time.

application of the *P* and *S* wave partial-offset stacking methods with swath 3-D MCS data to qualitatively image melt-rich and melt-poor sections of the AML at the EPR R2K ISS (~9°30′N–10°00′N; Figure 1b).

Figure 4 shows two CMP bin supergathers constructed by combining 12 consecutive CMP gathers from in-line 40 of box AXS and the corresponding *f-k* filtered supergathers. Clear $P_{AML}P$ waves at ~4.0 s two-way travel time (TWTT) within shot-receiver offsets of ~0–4 km (Figures 4c and 4d). After *f-k* filtering, CMP bin supergather 356098 also shows a coherent event between 2 and 4 km offsets observed at ~0.2 s below the $P_{AML}P$ waves (Figure 4c) that was difficult to identify in the unfiltered gather (Figure 4a). Based on its travel time and AVO behavior, we interpret this phase as a conversion from an incident *P* wave to an *S* wave reflected at the top of the AML and then converted back to a *P* wave at the seafloor ($P_{AML}S$ waves; Figure 4e). Other possible origins for this event, such as a peg-leg multiple from layer 2A or an *S* wave conversion at the base of layer 2A, do not predict the observed travel time and AVO behavior with offset. The comparison between CMP bin supergathers 356098 and 354229 shows that the character of the AML-reflected phases vary beneath different sections of the ridge (Figure 4). At CMP bin supergather 354229, the $P_{AML}P$ reflection is a strong event out to at least 4 km range, and there is no detectable $P_{AML}S$ reflection (Figures 4d and 4f), whereas the amplitude of the $P_{AML}P$ reflection at CMP bin supergather 356098 decreases beyond ~2 km range, and there is a strong $P_{AML}S$ reflection with an amplitude comparable to the $P_{AML}P$ reflection present at ~2–4 km offset range (Figures 4c and 4e). Based on the AVO predictions shown

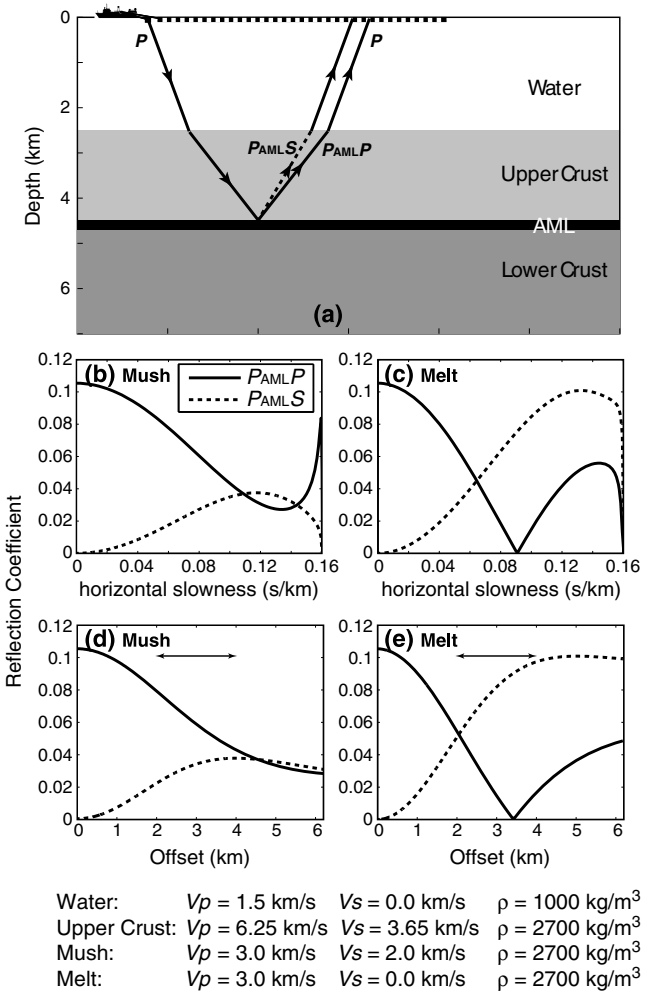

Figure 5. (a) Simplified cartoon of oceanic crust layering and schematic raypaths for $P_{AML}P$ and $P_{AML}S$ reflections. Model parameters are listed below. Two cases are shown, the mush case is for $Vs = 2.0$ km/s within the AML, while the melt case is for $Vs = 0$ km/s within the AML. (b and c) Absolute value of theoretically computed reflection coefficients (displacement) versus horizontal slowness. (d and e) Reflection coefficients plotted versus source-receiver offsets. We expect to see (1) that a phase reversal occurs for the $P_{AML}P$ reflection in the melt case and (2) that $P_{AML}S$ has a much higher reflection coefficient in the midoffset in the case of melt than in the mush case. The observation of high-amplitude $P_{AML}S$ and low-amplitude $P_{AML}P$ reflections at offset ~2–4 km can be used for partial-offset stacking to identify the presence of melt.

in Figure 5, these qualitative observations point to the presence of a large-melt fraction at CMP bin supergather 356098 and mush at CMP bin supergather 354229.

From the theoretical calculations of the AVO behavior of the AML reflection for melt and mush cases described above (Figure 5), it is clear that the crucial offset range for discriminating between the two representative cases is ~2–4 km. For a melt-rich sill, at these offsets, the amplitude of the $P_{AML}P$ waves decreases and eventually reverses polarity, and the amplitude of the *S*-converted $P_{AML}S$ waves increases. We constructed three partial-offset stacks: (1) 0–2 km offsets and constant NMO velocity (V_{NMO}) of 2.6 km/s that we call "$P_{AML}P$ near-offset stack," (2) 2–4 km offsets and $V_{NMO} = 2.6$ km/s that we call "$P_{AML}P$ midoffset stack," and (3) 2–4 km offsets and $V_{NMO} = 2.4$ km/s that we call "$P_{AML}S$ midoffset stack."

The resulting *P* and *S* wave-migrated stacks of the AML are illustrated in Figures 6a and 6b with one example in-line from each of the two swath 3-D boxes. These vertical sections of the partial-offset stack volumes show along-axis variations in the strength of the near-offset and midoffset $P_{AML}P$ reflection, as well as the variations in the presence of the $P_{AML}S$ event, suggesting along-axis variability in the physical properties of the AML. To make use of the full 3-D data contained in the seismic volumes and ensure that the interpretation of the along-axis variability in the $P_{AML}P$ and $P_{AML}S$ events is not biased by the choice of a specific in-line, we calculate the seismic energy of each trace within the volume and project it onto the in-line direction (Figures 6c and 6d).

The near-offset $P_{AML}P$ reflection is observed at ~4.0–4.1 s TWTT along most of the study area. The midoffset $P_{AML}S$ (~4.2–4.3 s TWTT) is observed along large parts of the profile, but it is strongest at four distinct sections (Figure 6). As expected, the stacked $P_{AML}S$ reflection is strong near CMP bin supergather 356098, and the amplitude of the midoffset $P_{AML}P$ reflection is greatly decreased compared to the near offset. The AVO behavior of the AML reflections shown in CMP bin supergather 356098 is used as our criterion to define melt-rich sections in this study. These melt-rich sections are primarily defined by the presence of strong energy in the *S* wave images (Figures 6c and 6d, third panels). Based on this criterion, we find four prominent 2–4 km long melt-rich zones spaced 5–10 km from each other at ~9°42′N–9°44′N, 9°47′N–9°48′N, 9°51′N–9°52′N, and ~9°57′N–9°58′N (Figures 1b and 6). While other reflections with similar characteristics

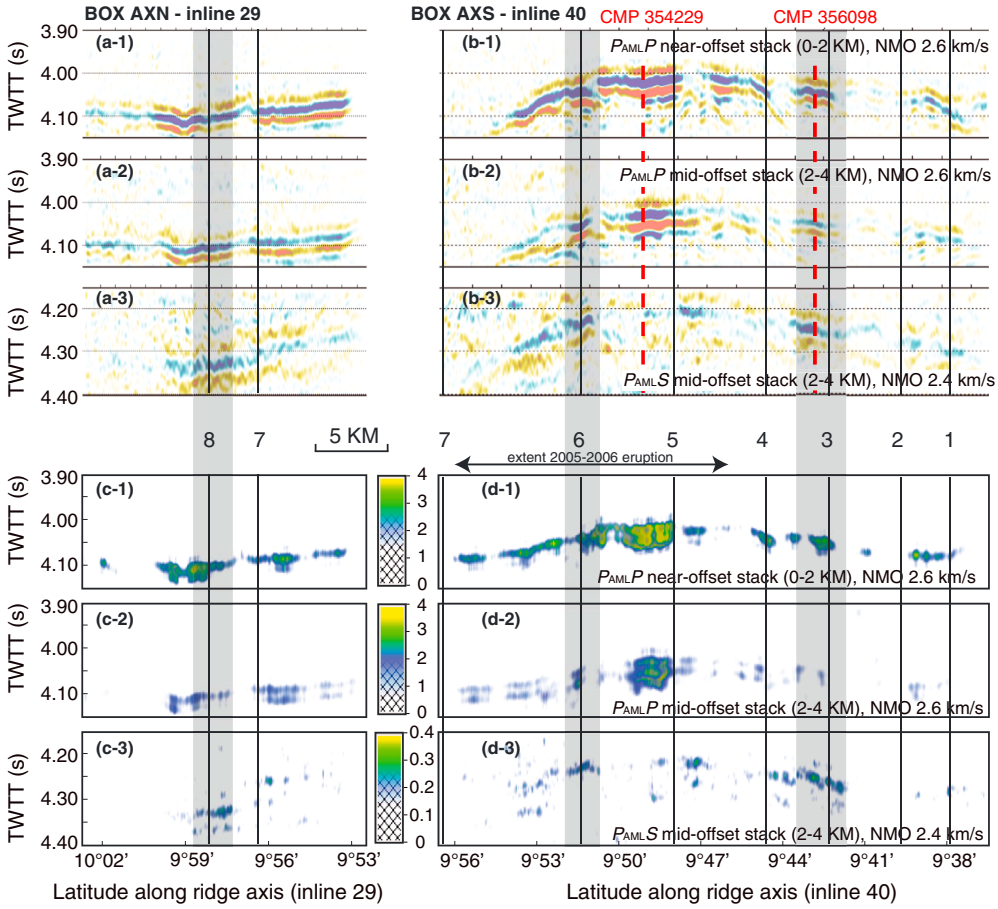

Figure 6. Partial-offset stacks. (a) In-line 29 for swath 3-D box AXN. (b) In-line 40 for swath 3-D box AXS. (c and d) Energy attribute of the whole poststack time-migrated volumes, projected onto in-lines AXN 29 and AXS 40, respectively. Gray shading highlights the presence of strong $P_{AML}S$ reflections with changes in $P_{AML}P$ waves amplitude between near-offset and midoffset stacks. These sections are interpreted as melt-rich sections in this study. Red dashed lines indicate the locations of the two CMP bin supergathers shown in Figure 4 and used for 1-D waveform modeling. Numbered vertical solid lines locate the center of the AML discontinuities identified by *Carbotte et al.* [2013]. Note that the location of these discontinuities may not exactly correlate with the AML discontinuities observed in Figure 6b (first panel), because the discontinuities of *Carbotte et al.* [2013] are not perpendicular to the ridge but rather oblique zones of finite width (up to 1.5 km), and they were defined from an along-axis MCS profile running along the center of the AST. The first to third panels in Figures 6a–5d show near-offset $P_{AML}P$, midoffset $P_{AML}P$, and midoffset $P_{AML}S$ stacks, respectively.

arepresent at similar depth at other parts of the segment, they are more ambiguous and lack the lateral continuity of the $P_{AML}S$ reflection mentioned above, so we will not attempt to interpret them any further.

5. Waveform Inversion

The *P* and *S* wave partial-offset stacks (Figure 6) described above provide an efficient way to constrain the length scales of variations in AML properties along a large portion of the ridge. However, they do not provide constraints on the fine-scale physical properties of the AML that produce the observed variations. To this end, we conducted a 1-D waveform inversion of *MGL0812* MCS data selected from two locations with contrasting melt content (as inferred from the partial-offset stacks), where the AML is best imaged: CMP 356098 located within a melt-rich section and CMP 354229 located within a melt-poor section at the site of the 2005–2006 eruption near a cluster of hydrothermal vents (Figure 1b).

5.1. The $\tau - p$ Transform

The mapping of intercept time-slowness ($\tau - p$) seismic data into the frequency (ω) domain is particularly useful for 1-D seismic analysis, since it decomposes the medium response into a series of noninteracting

cylindrical waves [*Harding*, 1985]. We follow the approach of *Korenaga et al.* [1997] to transform the time-offset (*t-x*) data to the $\tau - p$ domain. Incompleteness of field data (finite time, offset, and bandwidth) results in transform artifacts, which must be minimized for successful waveform inversion [*Korenaga et al.*, 1997]. Details of the tests performed to find the appropriate parameters for the $\tau - p$ transformation are given by *Xu* [2012]. Based on those tests, we restrict our analysis to traces within a slowness window from 0.01 to 0.158 s/km (mainly constraining the AML structure) for the 1-D waveform inversion. For $p > 0.16$ s/km, the transform produces artifacts with slope similar to that of the AML-reflected phases [*Xu*, 2012].

Figures 7c and 7d show the results of the $\tau - p$ transform of the two CMP bin supergathers shown in Figures 7a and 7b, respectively. Thirty-eight $\tau - p$ traces with slowness of 0.01–0.158 s/km and a frequency range of 5–30 Hz are used for the following waveform inversions. Because of the relatively small slownesses used in this study, we did not correct for source and receiver directivity effects (which discriminates against waves with large slowness) [e.g., *Collier and Singh*, 1997].

5.2. Full Waveform Inversion

The full waveform inversion method is described in detail by *Kormendi and Dietrich* [1991], and further information on the inversion procedure can be found in *Collier and Singh* [1997], *Korenaga et al.* [1997], and *Minshull et al.* [1994]. We give only a brief outline here; more details can be found in *Xu* [2012]. The waveform inversion scheme was designed to find the 1-D velocity structure that minimizes the misfit between the observed and predicted seismograms in frequency-slowness ($\omega - p$) domain. Synthetic seismograms were calculated using the generalized reflection transmission matrix method of *Kennett and Kerry* [1979], and the partial derivatives for the conjugate gradient algorithm were calculated from an analytical expression given by *Kormendi and Dietrich* [1991].

5.3. Source Wavelet

The inversion results are highly sensitive to the input source wavelet. Since we do not have field measurements of the far-field response of the air gun signal for our experiment, the source wavelet used for the inversion was obtained following an indirect approach [*Collier and Singh* [1997], method 4]. We estimated the source wavelets (Figures 7e and 7f) by averaging 10 $\omega - p$ traces at the lowest slowness (i.e., from 0.01 to 0.046 s/km) and then transformed the resulting averaged spectrum back to the $\tau - p$ domain.

5.4. Starting Model

The starting model consists of a stack of 8 m thick layers, for which *Vp*, *Vs*, density (ρ), and attenuation (Q) are defined. The thickness of 8 m was chosen so as to be less than one quarter of a wavelength for the maximum frequency used in the inversions, which is required for the precise computation of the synthetics [*Chapman and Orcutt*, 1985]. The limited bandwidth used makes the inversion procedure more stable, but at the expense of limiting the vertical resolving power of the method. For a maximum frequency of 30 Hz, the vertical resolution at the AML is limited to one fourth of the wavelength, which for $Vp = 3$ km/s is 25 m.

We used initial *Vp* models (Figures 7g and 7h) obtained from forward modeling of travel times of the seafloor reflection, layers 2A and 2B reflections and refractions, and the AML reflections for both CMP bin supergathers (Figures 7a and 7b). Density (ρ) was defined from the initial *Vp* structures using a *Vp*-ρ relationship [*Carlson and Raskin*, 1984], except at the seafloor and within the AML, where densities were set to 2240 kg/m^3 [*Gilbert and Johnson*, 1999] and 2700 kg/m^3 [*Hooft and Detrick*, 1993], respectively. *Vs* structures were derived from the initial *Vp* structures assuming a Poisson's ratio structure as described below.

For CMP bin supergather 356098, Poisson's ratio was set to be 0.48 for the upper 180 m and 0.29 elsewhere [*Christeson et al.*, 1997, 1996; *Hyndman and Drury*, 1976] (Figure 7g). The value of 0.29 was chosen to best fit the travel time of the $P_{AML}S$ reflection. The *P* wave attenuation quality factor (Q_p) was set to 16 in the upper 180 m and 100 below this depth [*Christeson et al.*, 1994] (Figure 7g). The high level of attenuation in the uppermost crust results from the combined effect of frictional, fluid flow, and scattering mechanisms [*Christeson et al.*, 1994; *Toksöz et al.*, 1987; *Wilcock et al.*, 1995].

For CMP bin supergather 354229, Poisson's ratio was set to be 0.48 for the upper 200 m and 0.29 elsewhere [*Christeson et al.*, 1997, 1996; *Hyndman and Drury*, 1976] (Figure 7h). To fit the amplitudes of seafloor and AML reflections, Q_p was set to 80 in the upper 200 m [*Wepfer and Christensen*, 1991] and to 500 below this depth, a value representative of off-axis lower crust [*Wilcock et al.*, 1995] (Figure 7h). These

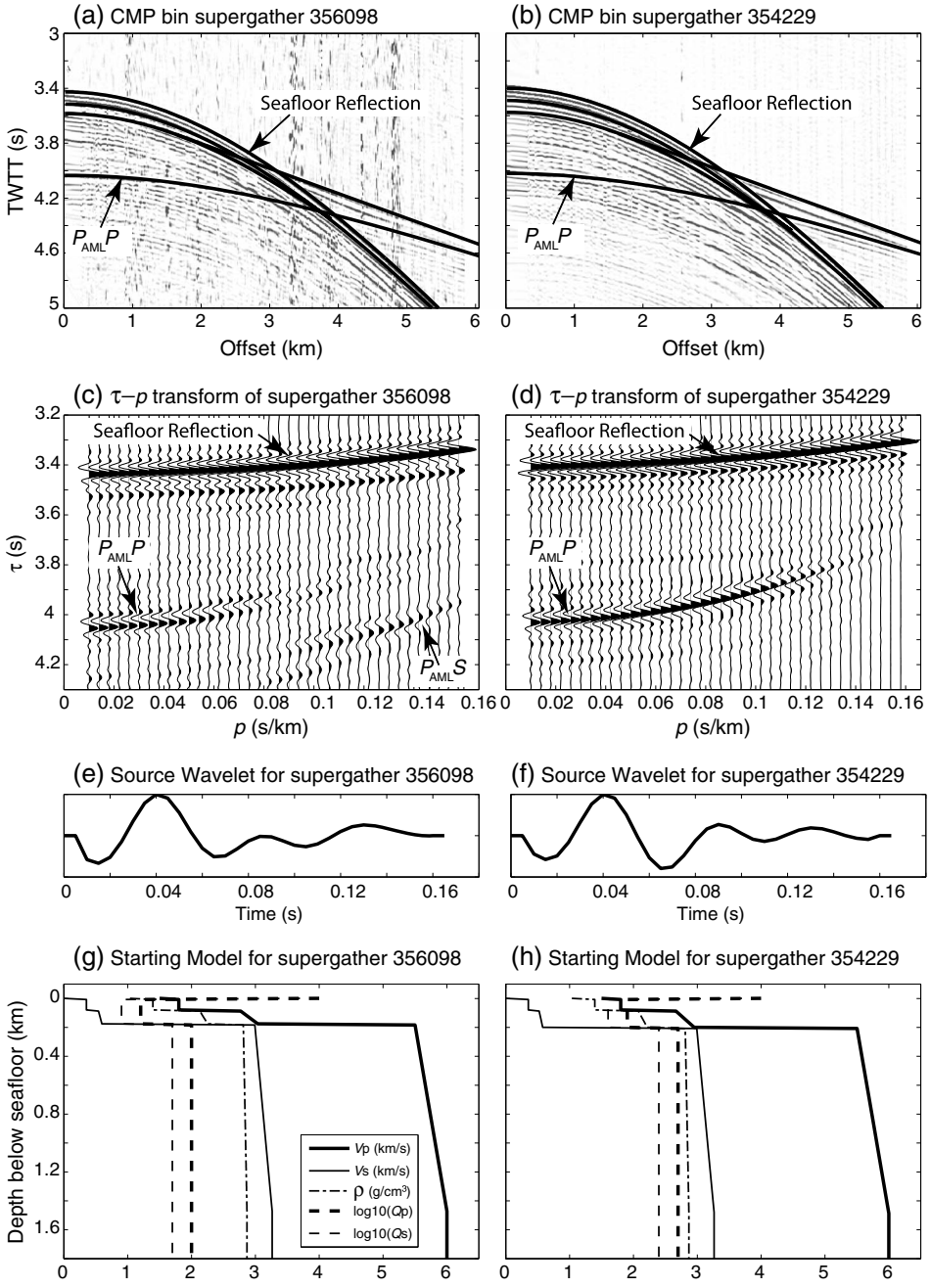

Figure 7. CMP bin supergathers from (a) the melt-rich section (356098) and (b) the melt-poor section (354229). (c and d) Corresponding $\tau - p$ transformed gathers, with seafloor, $P_{AML}P$ and $P_{AML}S$ reflections, are indicated by arrows. Note that CMP bin supergather 356098 shows a strong $P_{AML}S$ reflection (accompanied by a rapid decrease in $P_{AML}P$ amplitude) in the slowness range of 0.058–0.158 s/km, while CMP bin supergather 354229 does not show a detectable $P_{AML}S$ reflection. (e and f) Estimated source wavelets for CMP bin supergathers 356098 and 354229, respectively. (g and h) Starting models for the 1-D waveform inversion. The travel time curves calculated from starting models in Figures 7g and 7h used for 1-D waveform inversion are shown in bold lines. The starting *Vp* models were derived from fitting the main seismic phases shown in Figures 7a and 7b (see text for details). Units of *x* axis are indicated in the legend.

values are 5 times greater than the values for CMP bin supergather 356098. The reason(s) why data from these two locations require different attenuation structure above the AML are unclear and beyond the scope of this paper. One possibility is that the relatively low attenuation at CMP bin supergather 354229 might be caused by the cooling effect from intense hydrothermal circulation here, since the attenuation

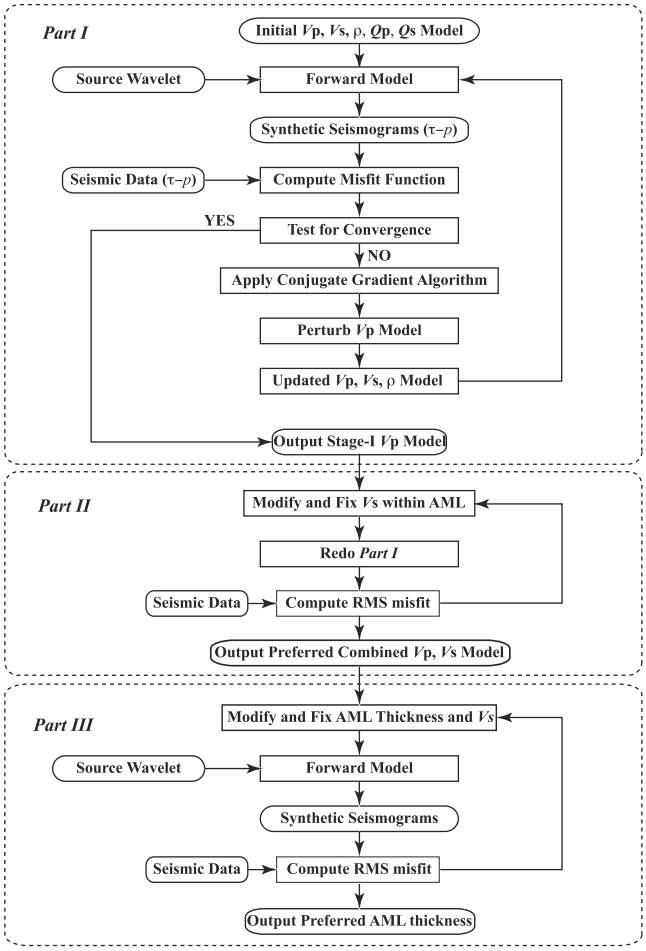

Figure 8. Schematic flowchart of the 1-D waveform inversion procedure applied in this study. The procedure includes three parts: part I is designed for obtaining an AML *Vp* model, part II is for estimating the AML *Vs*, and part III is for estimating the AML thickness.

quality factor is strongly dependent on temperature [*Kampfmann and Berkhemer*, 1985]. The *S* wave attenuation quality factor (Q_s) was set to half that of the *P* wave at both locations [e.g., *Tompkins and Christensen*, 2001].

5.5. Inversion Scheme

The 38 $\tau - p$ traces were inverted simultaneously. Therefore, the inverted model is consistent with the data from the range of slownesses modeled and is less likely to be influenced by incoherent noise [*Singh et al.*, 1998]. In this study, the model parameter in the full waveform inversion is *Vp*; *Vs* and ρ were not inverted during the inversion procedure. To obtain the preferred *Vs* structure, we conducted a series of inversions for *Vp* with different fixed *Vs* values. The preferred *Vp* solution, the estimates of *Vs* within the AML, and the estimates of the sill thickness were obtained through a waveform inversion and forward modeling procedure involving three parts described below and summarized in Figure 8.

Part I: First, we ran a series of inversions to obtain an acceptable solution for *Vp*. After the iterative inversion converged, we updated *Vs* and ρ (as described in the previous section) and conducted another inversion for *Vp*. This procedure was repeated until updating *Vs* and ρ did not produce any additional convergence in a subsequent inversion. The final results from this step are what we call "stage I *Vp* models."

Part II: To constrain *Vs* within the AML, we conducted another set of inversions as described in Part I using a starting model, the stage I *Vp* model, resulting from Part I and testing different *Vs* values within the AML. The final results from this step are what we call "preferred combined *Vp* and *Vs* models."

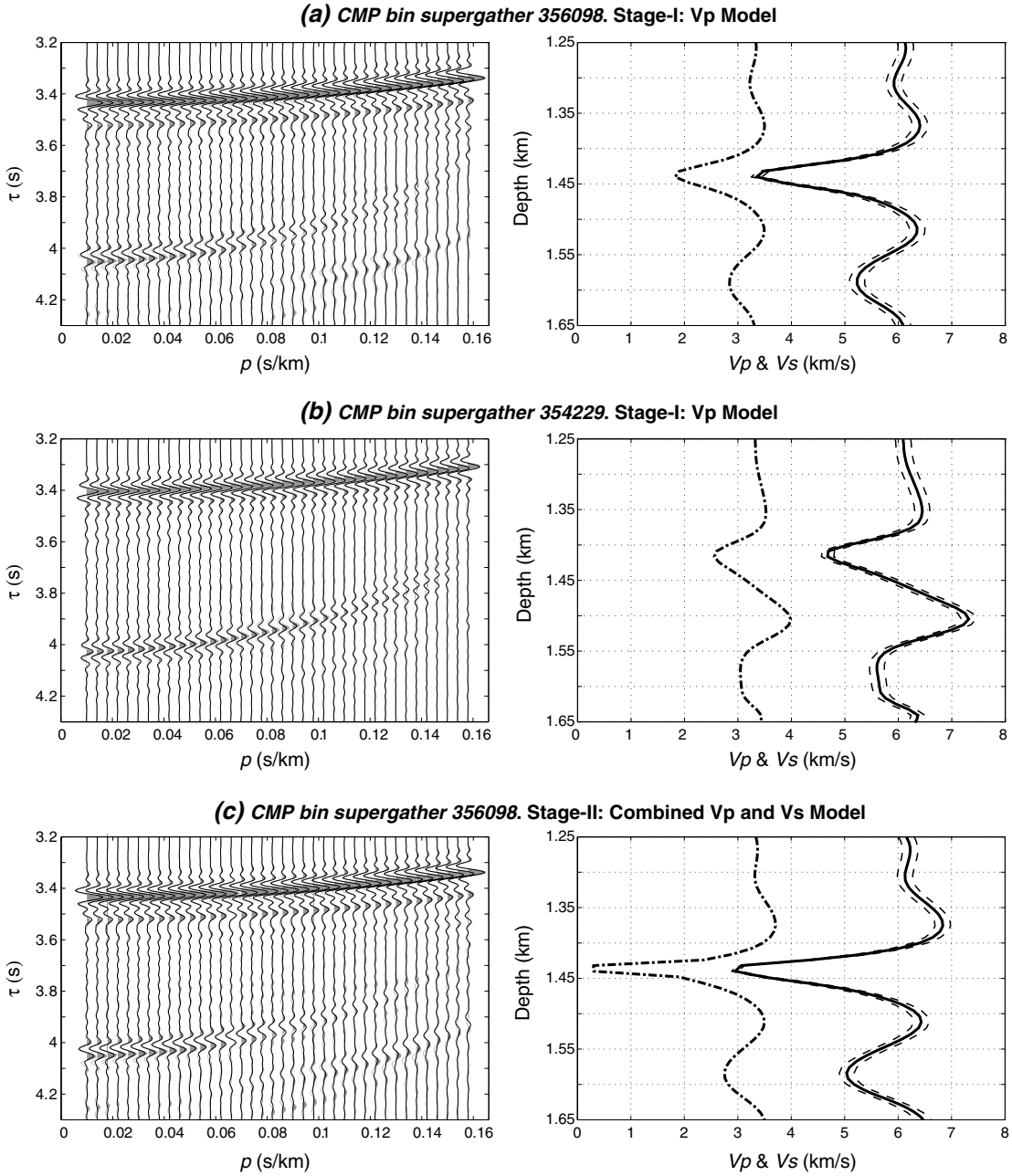

Figure 9. Results from stage I for (a) CMP bin supergather 356098 and (b) CMP bin supergather 354229, and results from stage II for (c) CMP bin supergather 356098. First column shows observed (gray) and predicted (black) $\tau - p$ traces. Second column shows *Vp* (solid lines) and *Vs* models (dash-dotted lines). Dashed lines show 1 standard deviation error estimated from the Hessian matrix of the *Vp* model.

Part III: In this last part, we constrained the thickness of the low-velocity AML. We conducted a set of forward models modified from with the preferred combined *Vp* and *Vs* models of Part II and testing different values for the AML thickness. These tests were repeated for several values of V_S within the AML to explore the full parameter space of AML thickness and V_S to assess any trade-off between these parameters.

5.6. Waveform Inversion Results

5.6.1. Part I: Stage I *Vp* Models

The stage I *Vp* models obtained from Part I of the inversion scheme as well as the predicted seismograms for CMP bin supergathers 356098 and 354229 are shown in Figures 9a and 9b, respectively. At the melt-rich site

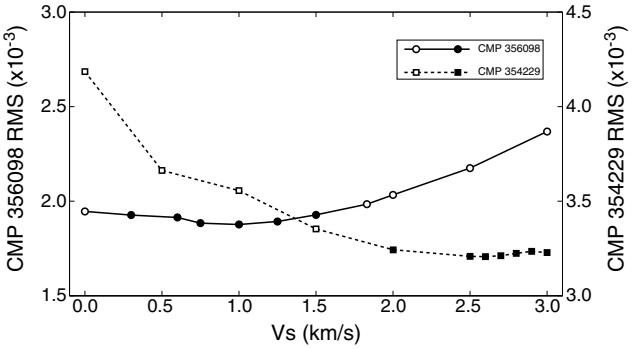

Figure 10. Results from stage II showing waveform RMS misfit versus AML V_S for CMP bin supergathers 356098 (open circles and solid line, scale on the left vertical axis) and 354229 (squares and dashed line, scale on the right vertical axis). Solid circles represent solutions, whose residuals are statistically indistinguishable (at the 90% significance level) from the solution with minimum RMS.

of CMP bin supergather 356098, results from stage I consist of an AML characterized by a tens-of-meters thick low-velocity zone, in which *Vp* decreases sharply from ~6.41 km/s to 3.35 km/s at 1.44 km depth.

At the melt-poor site of CMP bin supergather 354229, the inverted structure also contains a tens-of-meters thick low-velocity feature at a similar depth (1.41 km), but with a smaller decrease in *Vp* (from ~6.44 to 4.67 km/s). The stage I *Vp* models have an estimated uncertainty of 0.10–0.15 km/s (Figures 9a and 9b), which is valid only if the starting model is close to the global minimum of the misfit function.

5.6.2. Part II: Preferred Combined *Vp* and *Vs* Models

Our inversion approach only inverts for the *Vp* structure; thus, the V_S models of Figures 9a and 9b obtained in stage I largely reflect the a priori Poisson's ratio structure within the AML used as starting model. In order to better constrain the *Vs* structure within the AML, we proceeded with the inversion scheme Part II (Figure 8). Inversions were carried out with various, fixed values of *Vs* within the AML ranging between 0.0 and 3.0 km/s. For each inversion, we used the waveform RMS within the 3.7–4.3 s time window (which encompasses both $P_{AML}P$ and $P_{AML}S$ reflections; Figure 9) as a measure of the data misfit of each model. For CMP bin supergather 356098, the RMS misfit generally increases with increasing V_S, and the best fit is found for $V_S = 1.0$ km/s (Figure 10). To evaluate the statistical significance of each of the models, we conducted two sample Student's *t* tests comparing the waveform residuals of each model with those corresponding to the minimum RMS. The tests show that for CMP bin supergather 356098, waveform residuals obtained with V_S values between 0.3 and 1.5 km/s are statistically indistinguishable from each other at the 90% significance level (Figure 10). The *Vp* values for these models range between 2.95 km/s and 3.23 km/s, for $V_S = 0.3$ km/s and 1. km/s, respectively. We therefore chose *Vp* = 2.95–3.23 km/s and *Vs* = 0.3–1.5 km/s as our ranges of preferred AML models for CMP bin supergather 356098. Figure 9c shows one end-member of this range of preferred models ($V_S = 0.3$ km/s) and the corresponding predicted waveforms.

For CMP bin supergather 354229, the RMS misfit shows a different behavior, generally decreasing with increasing V_S, and the best fit is found for $V_S = 2.6$ km/s (Figure 10). The Student's *t* tests show that solutions with $V_S \geq 2.0$ km/s are all statistically indistinguishable from each other at the 90% significance level (Figure 10). For these AML models, *Vp* ranges between 4.52 km/s and 4.82 km/s for $V_S = 2.5$ km/s and 3.0 km/s, respectively. We therefore chose *Vp* = 4.52–4.82 km/s and *Vs* = 2.0–3.0 km/s as our ranges of preferred models for CMP bin supergather 354229. The model obtained during stage I for this site falls within this range of models; thus, results shown in Figure 9b belong to the family of preferred solutions.

5.6.3. Part III: Estimate of AML Thickness

The observation of the $P_{AML}P$ reflection in the frequency band (5–30 Hz) considered in this study (Figures 4 and 7) implies that the AML has a finite minimum thickness. Our synthetic tests indicate that to be observed in the 5–30 Hz frequency band, the AML has to be at least 8 m thick; thinner structures would be seismically transparent at those frequencies. Based on this, we choose 8 m as our estimate for the lower bound of the AML thickness.

In order to constrain the upper bound of the AML thickness, we calculated a series of synthetics (Part III; Figure 8) using velocity models that were modified versions of the preferred combined *Vp* and *Vs* models. The modifications were done by changing the thickness of the layer, where the *Vp* value is at its minimum (which we call "AML thickness"). Since the vertical resolution of our method is 25 m, we tested the AML thickness values distributed between 24 and 128 m at regular intervals of 8 m. To account for trade-offs in data misfit between AML thickness and *Vs*, we conducted a search for the best fit AML thickness for a variety of *Vs* values ranging between 0.0 and 3.0 km/s. This allowed us to explore the full parameter space for both thickness and *Vs*.

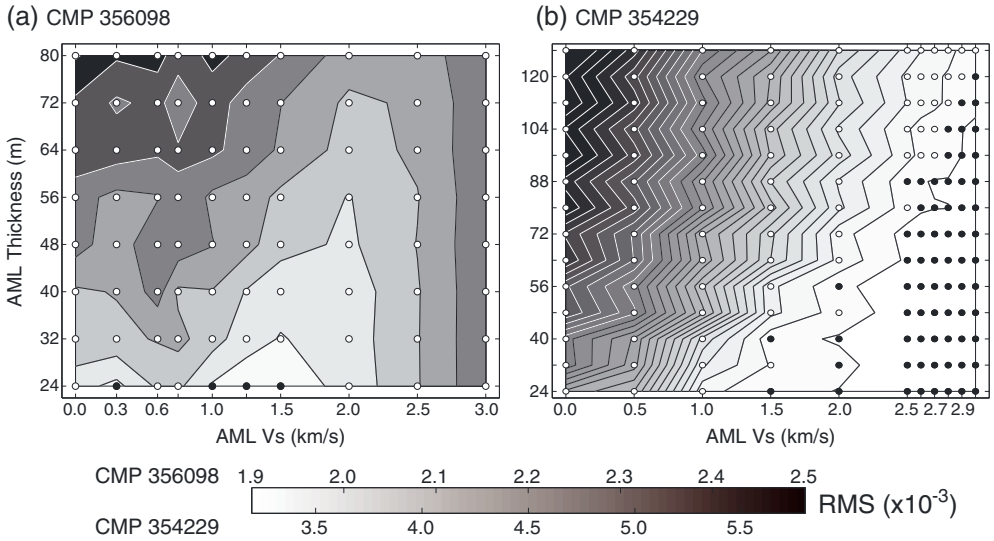

Figure 11. Results from stage III showing waveform RMS misfit as a function of both AML V_S and thickness for CMP bin supergathers (a) 356098 and (b) 354229. Open circles indicate the space of parameters explored. Solid circles represent solutions, whose residuals are statistically indistinguishable (at the 90% significance level) from the solution with minimum RMS. RMS is contoured every 0.1×10^{-3}.

Results for CMP bin supergather 356098 (Figure 11a) show that the best fit corresponds to an AML thickness of 24 m (and *Vs* between 0.3 and 1.5 km/s). AML thickness of 32 m or larger results in waveform residuals with RMS misfit that are statistically different and larger than those for 24 m. Therefore, at this location, we choose an AML thickness of 8–32 m as our preferred estimate.

For CMP bin supergather 354229, we find that waveforms are equally well fit for a much wider range of AML thickness (and for $Vs > 2.0$ km/s) (Figure 11b). We conclude that AML thickness at this location is more weakly constrained, with preferred estimates of 8–120 m.

5.7. Robustness of the Solutions

Investigations at the southern EPR (14°18–24′S) have shown that there, the melt lens is bounded by a solid roof and a solid floor [*Singh et al.*, 1999]. Our preferred *Vp* models (Figure 9) are consistent with these previous results; however, some of the features of these models may be dependent on the initial assumptions or not strongly constrained by the data [e.g., *Canales et al.*, 2006]. Here we investigate the robustness of the structure immediately beneath the melt lens, and its dependence on initial assumptions.

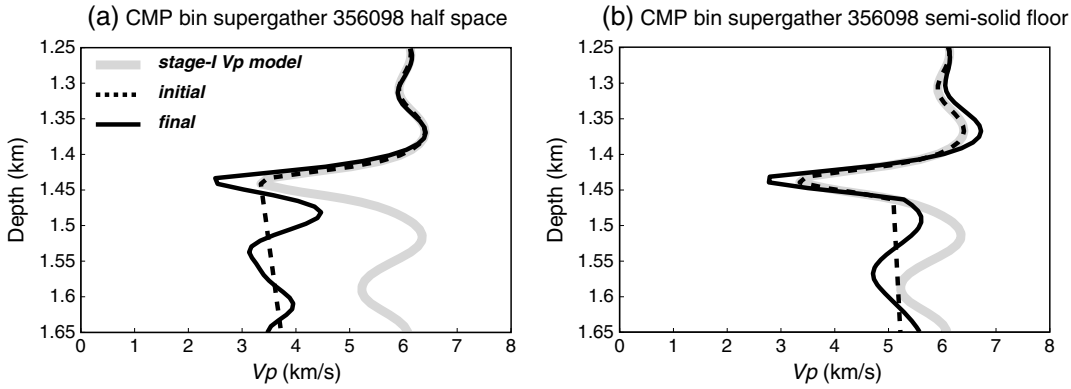

Figure 12. Tests for the robustness of the stage I *Vp* solution for the structure of the melt lens for CMP bin supergather 356098: (a) a purely molten half-space model modified from the stage I *Vp* model (Figure 9a, thick gray line) is used as an initial model (dashed line); black line shows the final inversion result. (b) Same as Figure 12a with an initial model assuming a partially molten floor.

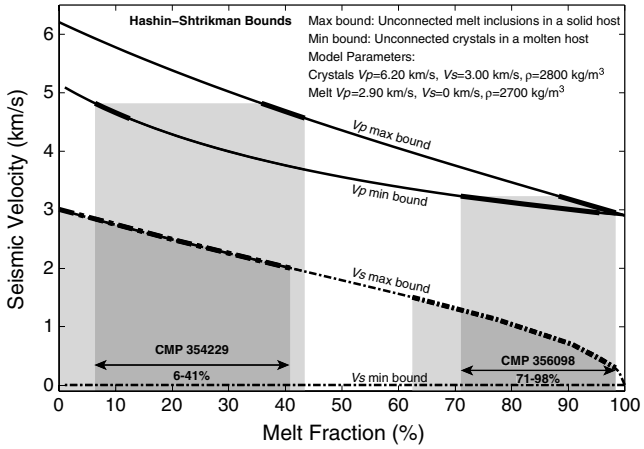

Figure 13. Hashin–Shtrikman bounds on seismic velocities for a two-phase material (melt and crystals in this study). The *Vp* and *Vs* bounds are shown in solid and dash-dotted lines, respectively. The shaded blocks indicate the inferred melt fraction ranges based on our preferred *Vp* and *Vs* models for CMP bin supergathers 356098 and 354229, respectively. The overlapping area between the *Vp*- and *Vs*-inferred melt fractions gives the range of preferred melt fraction estimates. Model parameters used from calculating the Hashin–Shtrikman bounds are listed in the figure.

We performed two series of inversions with different constraints to investigate the necessity of having a solid floor. We inverted the data from CMP bin supergather 356098 (melt-rich case) using initial velocity models modified from the stage I *Vp* model (Figure 9a): one where *Vp* is low everywhere beneath the AML (Figure 12a) and one in which the velocity of the melt lens floor increases moderately, simulating a semisolid floor (Figure 12b). In both cases, the new inversions result in models that fit the data with the same degree of accuracy as the stage I model, but that are far from the stage I result. Therefore, we conclude that although the data require an increase in *Vp*, with respect to the initial velocity model immediately beneath the melt lens, we cannot discriminate between a solid and a semisolid floor. Thus, our tests indicate that the AML is a partially molten thin lens overlaying a more crystalline medium, but the structure of this medium is unconstrained.

6. Discussion

6.1. Nature of the AML as of Summer 2008

6.1.1. Melt Content of the AML

The preferred *Vp* and *Vs* structures of the AML obtained from the 1-D waveform inversion procedure provide constraints on the crystallinity of the melt lens. The relationship between elastic parameters and melt fraction is not straightforward, and several authors have addressed this problem from different perspectives [e.g., *Dunn et al.*, 2000; *Mainprice*, 1997; *Taylor and Singh*, 2002]. Here we chose the statistical approach derived from effective medium theory, Hashin–Shtrikman bounds [*Hashin and Shtrikman*, 1963], to compute the upper and lower velocity bounds for a constant melt fraction (Figure 13). The maximum bounds correspond to an end-member model of unconnected melt inclusions in a solid host, and the minimum bounds represent the opposite end-member model of unconnected crystals in a molten host. There are six model parameters used for calculating the Hashin–Shtrikman bounds: *Vp*, *Vs*, and ρ for both crystals and pure melt. We tested different combinations of these parameters. For the melt-rich site, melt fraction is primarily constrained by *Vs*, and the choice of the other parameters do not significantly affect the estimation of melt fraction. For the melt-poor site, a melt fraction estimate is more sensitive to the choice of model parameters, resulting in a melt fraction estimate uncertainty of about 10%. In this study, we chose $Vp = 6.2$ km/s, $Vs = 3.0$ km/s, and $\rho = 2800$ kg/m^3 for the crystals and $Vp = 2.9$ km/s, $Vs = 0$ km/s, and $\rho = 2700$ kg/m^3 for the pure melt.

At the melt-rich site (CMP bin supergather 356098), the preferred range of *Vs* values (0.3–1.5 km/s) corresponds to melt fractions of 62–98%, while the preferred range of *Vp* values (2.95–3.23 km/s) indicates 71–98% melt. In contrast, at the melt-poor site (CMP bin supergather 354229), the larger *Vs* (2.0–3.0 km/s) suggests 0–41% of melt content, while *Vp* (4.52–4.82 km/s) is consistent with a magma body with 6–43% melt content (Figure 13). We chose the intersection between the *Vp*- and *Vs*-constrained melt fraction ranges as our best estimates of AML melt content: 71–98% at the melt-rich site and 6–41% at the melt-poor site.

These two estimates of melt content within the AML (Figure 13), together with the results from *P* and *S* wave partial-offset stacking (Figure 6), provide a more complete picture of the along-axis variation of the internal properties of the AML. Within the melt-rich sections, where both $P_{AML}P$ and $P_{AML}S$ events are well imaged and laterally continuous, the melt fraction in the AML is high (>70%), indicating that it could be nearly fully

molten. In contrast, within the melt-poor sections, where the $P_{AML}P$ event is well imaged, but the $P_{AML}S$ event is absent (indicating efficient propagation of shear energy though the AML), the AML is a partially molten solid with an intermediate-to-low melt fraction (<40%).

6.1.2. Spatial Variations of Melt Content Within the AML

Combining the results of qualitatively imaging melt-rich and melt-poor sections from *P* and *S* wave partial-offset stacks and the melt content estimates from the seismic velocities obtained from 1-D waveform inversion, we find that over the 60 km long section of the northern EPR studied here (~9°30′N–10°00′N), there are four prominent 2–4 km long melt-rich to fully molten sections contained within an otherwise melt-poor AML (Figures 1b and 6). The melt-rich sections are spaced every ~5–10 km along the ridge axis, which is about half of the spacing found for the southern EPR (~15–20 km; [*Singh et al.*, 1998]) and comparable to the fine-scale AML segmentation in this area reported by *Carbotte et al.* [2013] (5–15 km; Figure 6).

The small-scale, melt-mush segmentation provides insight into the melt delivery, eruption history, hydrothermal activity, and crustal accretion along the spreading axis. The melt-rich sections may correspond to the zones of fresh magma supplied from the mantle and more capable of erupting, or alternatively to sections of the ridge, where magma experiences less cooling and longer residence times. The more crystalline sections may have undergone more efficient or longer periods of cooling and crystallization [*Singh et al.*, 1998] or alternatively, they may represent sections of the ridge, where the AML has yet to be replenished after a recent eruption. These hypotheses are discussed in more detail in section 6.2. Furthermore, these along-strike variations in the AML melt content may be another factor contributing to inhibit—or resulting from limited—large-scale mixing or flow of magma along the ridge axis, as inferred from the geometrical segmentation of the AML and seafloor lava chemistry [*Carbotte et al.*, 2013].

Based on the melt content estimates from the seismic velocities (Figure 13), we suggest that >70% melt fraction could be present in the melt-rich sections and <40% melt fraction in the melt-poor sections. Over this 60 km long section of the EPR (9°30′N–10°00′N), melt-poor sections inferred from our partial-offset stacking results occupy >75% of its length. Assuming that the crystallinity in the AML melt-poor sections is too large for supporting eruptions without the occurrence of a new influx of melt from the lower crust/mantle, then only ~25% of the ridge axis at a given time may be capable of producing diking and seafloor eruptions, with the remaining ~75% of the AML contributing primarily to the construction of the lower crust.

6.1.3. Comparisons With Previous Studies

Using data collected in 1985 and 1-D seismic waveform inversion, *Collier and Singh* [1998] estimated that at 9°48.5′N (their CMP 11050), the AML was characterized by $V_S < 1$ km/s, which led them to infer a high-melt content (~80 ± 10%) at this location. *Collier and Singh*'s [1998] CMP 11050 is located within one of the melt-poor sections found in our study, just over 1 km to the south from CMP bin supergather 354299, where we obtain $V_S = 2.5$–3.0 km/s.

Farther to the south at 9°39′N, *Collier and Singh* [1998] also obtained a low value for V_S (<1 km/s) and high-melt content at their CMP 10340. However, using the same 1985 data, but a different approach (waveform forward modeling as opposed to waveform inversion), *Hussenoeder et al.* [1996] obtained $V_S = 1.45$ km/s and therefore inferred a more crystalline AML. Contrasting with these two previous studies, we find that the absence of significant $P_{AML}S$ energy in our 2008 data at this latitude (Figure 6d, third panel) suggests higher V_S and therefore low-melt content. One could speculate that the different results obtained with the 1985 and 2008 data sets could reflect temporal variations on decadal time scales of the physical properties of the melt lens. However, given that the same 1985 data at 9°39′N gave different results depending on the modeling approach, a more likely explanation is that the studies of *Collier and Singh* [1998] and *Hussenoeder et al.* [1996] have large uncertainties in their melt content estimates due to the limited aperture of their 1985 data (2.4 km long streamer), which prevented them from using $P_{AML}S$ events for their analysis, as we have done in our study.

6.1.4. AML Thickness

Here we compare our seismically determined melt lens thicknesses (8–32 and 8–120 m; Figure 11) with estimates from field observations of ophiolites and other seismic studies. The study of ophiolites has played an important role in the development of models for MOR magma chambers [e.g., *Casey and Karson*, 1981; *Greenbaum*, 1972; *MacLeod and Yaouancq*, 2000; *Nicolas et al.*, 1988, 1993; *Pallister and Hopson*, 1981]. Arguably, the best analog for fast spreading crust is the Oman ophiolite. *Browning* [1984] and *Browning et al.* [1989] showed that the observed cryptic (mineral and chemical) variation of the cumulate layers within the cyclic layered gabbro sequences of the Troodos and Oman ophiolites is best modeled by the formation from

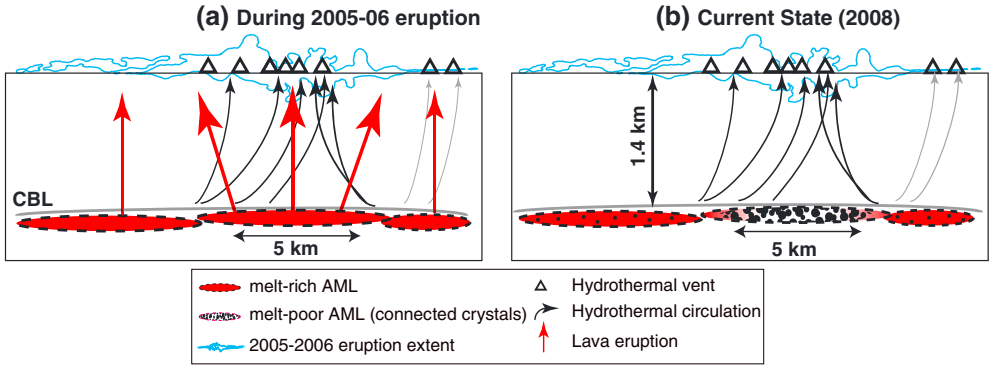

Figure 14. A cartoon showing our preferred scenario regarding the relationships between the physical state of the AML before and after the 2005–2006 eruption and hydrothermal activity. (a) The 2005–2006 eruption drained most of the melt in a 5 km long melt-rich section, which had been driving hydrothermal circulation in this area. (b) This left behind a large fraction of connected crystals separating the distal ends of the lens from which melt was not fully drained. The gray line above the AML represents a conductive boundary layer, which separates the hydrothermal circulation and the AML.

melt sills that are no more than about 100–200 m thick. From structural and petrological mapping of the upper gabbro and dike contact in the Oman ophiolite, *MacLeod and Yaouancq* [2000] proposed the presence of a 150 m thick fossil melt lens. However, a more recent series of detailed studies of the root zone of the sheeted dike complex and uppermost gabbros in Oman that have mapped a petrological boundary interpreted as formed at a fossil melt lens [*Boudier and Nicolas*, 2011; *Nicolas and Boudier*, 2011; *Nicolas et al.*, 2009, 2008] argue that the thickness of the paleomelt lens cannot be inferred, because as the crustal section drifted away from the axial region and the lens soldified, both the floor and roof of the melt lens became essentially a single interface [*Nicolas et al.*, 2009].

The thickness of MOR AMLs has been seismically investigated through waveform modeling and the analysis of the AVO behavior of AML reflections [e.g., *Canales et al.*, 2006; *Collier and Singh*, 1997; *Hussenoeder et al.*, 1996; *Kent et al.*, 1990; *Singh et al.*, 1998, 1999]. Along the northern EPR near 9°30′N, *Kent et al.* [1990] derived a lower bound on the thickness of the magma body by reflectivity modeling of the interference effects between a wavelet reflecting off the top and bottom of a thin layer of melt as its thickness decreases. A layer thickness of ~10–50 m is required to explain the lack of a distinct basal reflection in the observed data. However, the absence of this basal reflection can also be explained by a gradual increase in velocities across a transitional lower boundary of a thicker magma body due to a transition from melt to crystal mush. From their waveform modeling studies, *Hussenoeder et al.* [1996] and *Collier and Singh* [1997, 1998] also showed the thickness of the sill to be on the order of 30–80 m beneath the EPR at 9°48′N and 9°39′N. Similar results were obtained at the southern EPR [*Hussenoeder et al.*, 1996; *Singh et al.*, 1998, 1999], southern JdFR [*Canales et al.*, 2006], Valu Fa ridge in the Lau Basin [*Collier and Sinha*, 1990], and the East Scotia Ridge in the South Atlantic [*Livermore et al.*, 1997]. Our determined AML thicknesses (8–32 and 8–120 m) are consistent with the seismically determined thicknesses described above (<100 m), but thinner than estimates from ophiolite observations.

Previous studies based on modeling of refraction data suggested the presence of low velocities immediately above and below the melt sill [*Toomey et al.*, 1990; *Vera et al.*, 1990]. The low velocity just above the AML has been interpreted to be due to a thermal anomaly, and the low velocity below the AML is thought to represent a hot, partially molten mush zone underlying the melt sill [*Toomey et al.*, 1990; *Vera et al.*, 1990]. Our modeling results show that the thin AML is capped by a high *Vp* solid roof and underlain by a solid floor or semisolid floor (Figures 9 and 12).

6.2. Relations Between the Physical State of the AML Pre-2005–2006 and Post-2005–2006 Eruptions and Hydrothermal Activity

An important finding in our study is the observation that at the time of data acquisition in 2008, the section of the AML between 9°48 and 51′N near the center of the 2005–2006 eruption, which coincides with most of the AML segment 5–6 in the nomenclature of *Carbotte et al.* [2013], does not show high-melt content (despite including the highest-amplitude AML reflection found in our study area; Figures 6b-1 and 6d-1), while to the

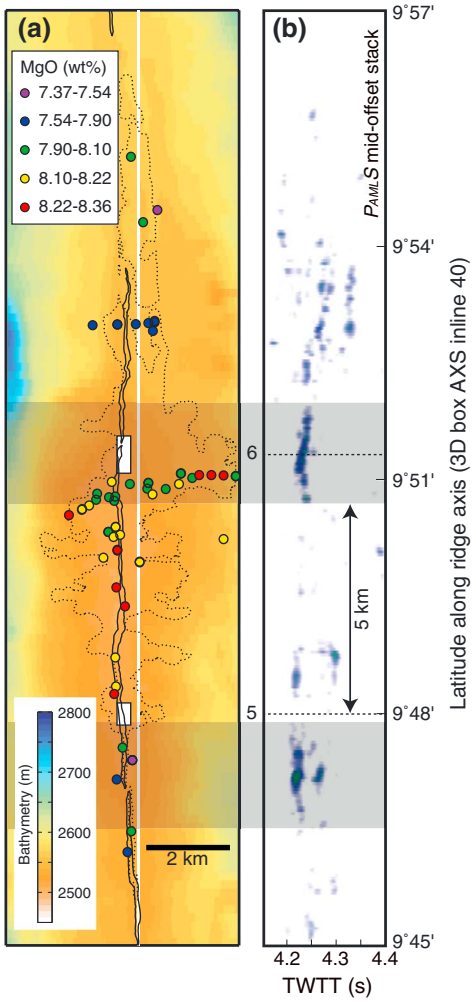

Figure 15. Correlation between the MgO wt % and melt-mush segmentation of the 9°45′N–9°57′N segment of the northern East Pacific Rise. (a) Bathymetry map showing the location of the axial summit trough (solid line) and the spatial extent of the 2005–2006 eruption (dotted line) [*Soule*, 2012; *Soule et al.*, 2007]. The basalt sample locations are indicated by solid circles, with colors showing the ranges of MgO wt % [*Goss et al.*, 2010]. Solid white line locates in-line 40 from the swath 3-D box AXS from which the example data are shown in Figure 6b. (b) Energy attribute of poststack time-migrated volume for midoffset *S* wave partial-offset stacks. Shading indicates the presence of strong *S*-converted waves that is interpreted as resulting from melt-rich sections of the AML. Note that samples with highest MgO content (i.e., higher solidus temperature [*Sinton and Detrick*, 1992]) correlate spatially with an ~5 km long gap in the presence of the $P_{AML}S$ event (i.e., melt-poor and cooler sections of the AML). We interpret this apparent paradox as indicating the section of the melt lens that contributed to the 2005–2006 eruption. Numbered dashed lines locate the center of *Carbotte et al.*'s [2013] AML discontinuities 5 and 6, which are shown as white rectangles in Figure 15a.

south and north of these latitudes, we infer high-melt content (Figures 1 and 6). Here we discuss the possibility that the along-axis melt content variation that we observe between 9°45′N and 9°57′N is a direct consequence of melt extraction from the AML during the 2005–2006 eruption. Based on the along-axis variations in melt content inferred from the partial-offset stacks within the 2005–2006 eruption site, we discuss two possible scenarios regarding the current physical state of the AML and the 2005–2006 eruption, and their implications for hydrothermal activity in this area (Figure 14).

On the basis of AML segmentation beneath the eruptive zone and spatial variations in lava geochemistry and the volume of erupted lavas, *Carbotte et al.* [2013] argue that three segments (4–5, 5–6, and 6–7; Figure 6) contributed to the 2005–2006 eruption. Here we argue that the contribution of the AML segments 4–5 and 6–7 to the eruption was probably minor, on the basis of our observation of melt-rich zones at AML discontinuity no. 6 (and possibly to the north of it; Figure 6) and beneath the southern end of the eruption zone (northern end of segment 4–5; Figure 6). Our assumption that the main source of the 2005–2006 eruption was located between 9°48′N and 51′N within the AML segment 5–6 is justified by the observations that the bulk of the axial lavas and the greatest abundance of high-flow rate lava morphologies were erupted between 9°48′N and 52′N [*Fundis et al.*, 2010; *Soule et al.*, 2007] and by the geochemical data indicating that this melt lens was actually hotter than the neighboring areas [*Goss et al.*, 2010]. Thus, we consider a first scenario (Figures 14) in which we assume that the main source of the 2005–2006 eruption was the ~5 km long melt-rich lens extending between 9°48′N and 51′N (AML segment 5–6 [*Carbotte et al.*, 2013]). We classify the current state (as of 2008) of this section of the AML as melt poor based on our partial-offset stacking (Figure 6). The eruption drained most of the melt in this 5 km long part of the AML segment 5–6, while the observation of strong *S* wave reflections off the AML in the partial-offset stacking at 9°51′N and 54′N (AML segment 6–7) and 9°47′N and 48′N (AML segment 4–5) (Figure 15b) indicates that the eruption did not fully drain these AML segments to the north and south (Figure 14b).

Table 3. Estimates of Melt Volume and 2005–2006 Eruption Parameters

Th[a] (m)	V[b] ($\times 10^6$ m^3)	M_{rich} (%)	M_{poor}[c] (%)	V_m^{rich}[d] ($\times 10^6$ m^3)	V_m^{poor}[d] ($\times 10^6$ m^3)	V_{ext}[e] ($\times 10^6$ m^3)	V_{dike}[f] ($\times 10^6$ m^3)	W_{dike}[g] (m)	ΔT[h] (yr)
10	30	71–98	6–41	21.3–29.4	1.8–12.3	9.0–27.6	<15.6	<2.2	<20
30	90	71–98	6–41	63.9–88.2	5.4–36.9	27.0–82.8	15.0–70.8	2.1–10.1	19–92
120	360	71–98	6–41	255.6–352.8	21.6–147.6	108.0–331.2	96.0–319.2	13.7–45.6	125–415

[a] Th: AML thickness.
[b] V: volume of AML segment.
[c] M: AML melt content.
[d] $V_m = V \cdot M$: volume of melt within AML segment.
[e] $V_{ext} = V_m^{rich} - V_m^{poor}$: volume of melt extracted from AML segment 5–6 during the 2005–2006 eruption (minimum and maximum estimates).
[f] $V_{dike} = V_{ext} - V_{seafloor}$: volume of dike emplaced above AML segment 5–6 during the 2005–2006 eruption (minimum and maximum estimates), where $V_{seafloor} = 12 \times 10^6$ m^3 is the volume of lava emplaced on the seafloor between latitudes 9°48–51′N during the 2005–2006 eruption.
[g] W_{dike}: dike width (minimum and maximum estimates).
[h] $\Delta T = W_{dike}/SR$: eruption interval (minimum and maximum estimates), where $SR = 0.11$ m/yr is spreading rate.

An alternative scenario is that the physical state of the AML prior to the 2005–2006 eruption was similar to what the posteruption partial-offset stacks indicate (Figures 6 and 15b). In this scenario, the 5 km long melt-poor section of segment 5–6 beneath the center of the eruption site could be attributed to sustained cooling by the intense hydrothermal activity that is focused in this region, which may prevent the formation of a melt-rich lens as predicted by some numerical models of hydrothermal fluid flow above the AML [*Fontaine et al.*, 2011]. The 2005–2006 eruption would then have been fed by melt accumulated south and north of the hydrothermal field, where hydrothermal cooling may have been less effective. The inference that these two melt sources for the 2005–2006 eruption have a very high melt content just 2 years after the eruption would indicate rapid refilling of the AML following an eruption, or that a small percentage of the AML melt was drained by the eruption.

Of those two hypotheses, we favor the first scenario for the following reasons: (1) The central eruption region (9°48′N and 51′N), which coincides with the AML segment 5–6, contains the thickest, most voluminous and far traveling lava flows, which erupted from a continuous axial fissure [*Carbotte et al.*, 2013; *Fundis et al.*, 2010; *Goss et al.*, 2010; *Soule et al.*, 2007], indicating that the primary vent for the eruption is within this region. (2) Geochemical data from two recent eruptions (1991–1992 and 2005–2006) show that segments 4–5, 5–6, and 6–7 have erupted lavas of different chemistry in both of the last eruptions, indicating that these three segments contributed to the eruption with lavas delivered vertically to the seafloor [*Carbotte et al.*, 2013]. (3) The documented compositional heterogeneity in the 2005–2006 lavas provides an evidence for along-axis variations in the extent of melt differentiation [*Goss et al.*, 2010]. Many of the 2005–2006 lavas from the central lens have the most primitive (highest MgO wt %; Figure 15a) and least fractionated major and trace element compositions of this eruption [*Carbotte et al.*, 2013; *Goss et al.*, 2010], suggesting that the melt within the underlying AML in this region is comparatively hot. These differences in crystallization conditions suggest that melts within the AML are somewhat cooler to the north, perhaps because of a less voluminous melt production in the underlying mantle or a less frequent supply of melt derived from the sub-AML mush zone.

All of the above reasons are consistent with the assumption of scenario 1 that the majority of the lava that erupted on the seafloor during the 2005–2006 eruption was drained from an ~5 km long section between 9°48′N and 51′N, which is now classified as melt-poor based on our analyses. Our results and other observations allow us to put constrains on the volume of magma involved in the eruption (Table 3). For our calculations, we use an average value of 600 m for the AML width, which is reported to be 500–700 m near 9°50′N [*Carton et al.*, 2010; *Harding et al.*, 1993]. We have constrained the thickness of the AML at the melt-rich site to be 8–32 m (Figure 11a). For simplicity, we assume that the average AML thickness along the 2005–2006 eruption site is also 8–32 m. Thus, in the following calculations and discussion, we consider two values for the AML thickness: 10 m and 30 m. (Results for the extreme case of an AML thickness of 120 m are listed in Table 3.)

Based on the above AML dimensions and assuming that the melt fractions calculated for melt-rich (71–98%) and melt-poor (6–41%) sections in the magma lens represent the melt content in the 5 km long lens (segment 5–6) prior to and after the eruption, respectively, we estimate the ranges of magma volume extracted from this lens of $9.0–27.6 \times 10^6$ m^3 and $27.0–82.8 \times 10^6$ m^3, for AML thicknesses of 10 m and 30 m, respectively (Table 3). Using the seafloor extent of the 2005–2006 eruption reported by *Soule et al.* [2007] and assuming an average flow thickness of 1.5 m [*Soule et al.*, 2007], we estimate that a volume of ~12×10^6 m^3 of lava was emplaced on the seafloor between latitudes 9°48′N and 51′N during the 2005–2006

eruption. This implies that for an AML thickness of 10 m, a volume of melt of $<15.6 \times 10^6$ m^3 was left in the upper crust as dikes above the AML segment 5–6, while a 30 m thick AML would yield a dike volume of $15.0–70.8 \times 10^6$ m^3. An interesting consequence of this scenario is that the 2005–2006 eruption ceased after 30–92% of the magma available in the AML was drained, which contrasts with the <15% of magma evacuated from the AML inferred by *Soule et al.* [2007], who assumed that the eruption was fed uniformly over an 18 km long section of the ridge.

We acknowledge two caveats regarding the estimates of the volume of melt left in the crust discussed above: on one hand, the volumes may be minimum estimates because the 2005–2006 eruption likely involved extraction of melt not only from the shallow AML but also from deeper crustal levels, with ~25% perhaps originating in the lower crust [*Wanless and Shaw*, 2012]. On the other hand, the volumes may be maximum estimates, because we are assuming that the eruption drained the full width of the AML; there is the possibility that only a narrow zone of the AML contributed to the eruption.

Assuming a maximum dike height of 1.4 km (i.e., depth to the AML), and a length of 5 km, then the estimated dike volumes correspond to a dike width of <2.2 m for a 10 m thick AML, which is comparable to the mean dike width (0.5–1.5 m) observed at ophiolites and tectonic windows into recently active spreading ridges [*Gudmundsson*, 1995; *Harper*, 1984; *Kidd*, 1977; *Oliver and McAlpine*, 1998; *Rosencrantz*, 1983; *Tryggvason*, 1994; *Umino et al.*, 2003], or a width of 2.1–10.1 m for a 30 m thick AML (Table 3). While the latter value seems large for a single dike, it could represent the cumulative thickness of several dikes.

The width of the dike can be taken as a measurement of the amount of plate separation accommodated during the 2005–2006 eruption. Therefore, an eruption of similar dimensions to the 2005–2006 one would be needed, on average, every <20 years or 19–92 years (depending on AML thickness; Table 3) in order to sustain the long-term averaged seafloor spreading rate of 110 mm/yr. These estimates are consistent with the time interval between the 1991–1992 and 2005–2006 eruptions, as well as with the previous estimates of yearly to decadal time scale estimates for eruption recurrence intervals at fast spreading ridges [e.g., *Perfit and Chadwick*, 1998].

7. Conclusions

We have used *P* and *S* wave partial-offset stacking to infer melt-rich and melt-poor sections along the northern EPR 9°30′N–10°00′N and 1-D waveform inversion to determine the physical properties of the AML at two locations with contrasting melt content. On the basis of the interpretations of the nature of the AML, correlations between melt-mush segmentation, hydrothermal activity and 2005–2006 lava eruption, and spatial variations of melt content within AML, we make the following conclusions:

1. Between 9°30′N and 10°00′N, the melt content of the AML varies along the EPR axis. We found four prominent melt-rich sections ~2–4 km long and spaced every ~5–10 km along the ridge axis.
2. The AML is located ~1.4 km beneath the seafloor. The AML reflections observed in the melt-rich sections are best modeled with a low *Vp* (2.95–3.23 km/s) and *Vs* (0.3–1.5 km/s) within an 8–32 m thick lens, while in the melt-poor sections, reflections are best modeled with a higher *Vp* (4.52–4.82 km/s) and *Vs* (2.0–3.0 km/s) within an 8–120 m thick lens.
3. The melt-mush segmentation, together with the melt content estimates obtained based on Hashin–Shtrikman bounds, indicate that the crystallinity of the AML varies along the ridge axis. Within the melt-rich sections, the melt fraction in the AML is estimated to be 71–98%. In contrast, within the melt-poor sections, the AML has a low-to-intermediate melt fraction (6–41%).
4. Over this 60 km long section (9°30′N–10°00′N), the presence of melt-poor sections inferred from partial-offset stacking occupies >75% of the length. This means that at a given time, <25% of the ridge axis is capable of producing diking and seafloor eruptions, with the remaining >75% of the AML contributing primarily to the construction of the lower crust.
5. Our results indicate that the main source of the 2005–2006 eruption was a 5 km long melt-rich section of the AML located between 9°48 and 51′N. The eruption drained most of the melt in this lens, leaving behind a large fraction of connected crystals separating the AML segments to the north and south from which melt was not fully drained.
6. The volume of the 2005–2006 eruption from the 5 km long section has been estimated using the mean values of AML dimensions (600 m wide and 10–30 m thick), and the 30–92% melt fraction decrease.

Our calculations suggests that between 9°48′N and 51′N, a volume of magma ranging between 9 and 83×10^6 m^3 was extracted from a 10–30 m thick, 5 km long lens, of which a maximum of 71×10^6 m^3 of magma was left unerupted in the crust as dikes no more than 10 m wide.

7. If the width of the dike represents a proxy for the amount of plate separation accommodated during the 2005–2006 eruption, then the long-term average seafloor spreading rate of this ridge segment could be magmatically sustained with the eruptions of similar dimensions occurring every 20 years or less (if the AML is 10 m thick), or with a frequency of a few-to-several decades if the AML is 30 m thick.

Acknowledgments

We are grateful to the captain, crew, technical staff, and scientific party of the R/V *Marcus Langseth* cruise *MGL0812* for their valuable assistance in collecting the MCS data used in this study. We thank R. Stephen, D. Lizarralde, and S.A. Soule for their insightful discussions. Constructive reviews by K.C. Macdonald and an anonymous referee helped improve the original manuscript. This research was supported by NSF grants OCE-0327885 and OCE-0327872 through the RIDGE-2000 program.

References

Aghaei, O., M. R. Nedimović, H. Carton, S. M. Carbotte, J. P. Canales, and J. C. Mutter (2014), Crustal thickness and Moho character of the fast-spreading East Pacific Rise from 9°42′N to 9°57′N from poststack-migrated 3D MCS data, *Geochem. Geophys. Geosyst.*, *15*, 634–657, doi:10.1002/2013GC005069.

Anderson, D. L., and H. Spetzler (1970), Partial melting and the low-velocity zone, *Phys. Earth Planet. Inter.*, *4*(1), 62–64.

Boudier, F., and A. Nicolas (2011), Axial melt lenses at oceanic ridge - A case study in the Oman ophiolite, *Earth Planet. Sci. Lett.*, *304*(3–4), 313–325.

Browning, P. (1984), Cryptic variation within the cumulate sequence of the Oman ophiolite: Magma chamber depht and petrological implications, in *Ophiolites and Oceanic Lithosphere*, *Geol. Soc. Spec. Publ.*, edited by I. G. Gass, S. J. Lippard, and A. W. Shelton, pp. 71–82, London, U. K.

Browning, P., S. Roberts, and T. Alabaster (1989), Fine-scale model layering and cyclic units in ultramafic cummulates from the CY-4 borehole, Troodos ophiolite: Evidence for an open system magma chamber, in *Drillhole CY-4, Troodos Ophiolite, Cyprus*, edited by I. L. Gibson et al., pp. 193–220, Geological Survey of Canada, Ottawa, Canada.

Canales, J. P., S. C. Singh, R. S. Detrick, S. M. Carbotte, A. J. Harding, G. M. Kent, J. B. Diebold, J. Babcock, and M. R. Nedimović (2006), Seismic evidence for variations in axial magma chamber properties along the southern Juan de Fuca Ridge, *Earth Planet. Sci. Lett.*, *246*, 353–366.

Canales, J. P., H. Carton, S. M. Carbotte, J. C. Mutter, M. R. Nedimović, M. Xu, O. Aghaei, M. Marjanović, and K. Newman (2012), Network of off-axis melt bodies at the East Pacific Rise, *Nat. Geosci.*, *5*(4), 279–283.

Carbotte, S. M., and K. C. Macdonald (1992), East Pacific Rise 8°–10°30′N: Evolution of ridge segment and discontinuities from SeaMARC II and three-dimensional magnetic studies, *J. Geophys. Res.*, *97*, 6959–6982.

Carbotte, S. M., M. Marjanovic, H. Carton, J. C. Mutter, J. P. Canales, M. R. Nedimović, S. Han, and M. R. Perfit (2013), Fine-scale segmentation of the crustal magma reservoir beneath the East Pacific Rise, *Nat. Geosci.*, *6*, 866–870.

Caress, D. W., M. S. Burnett, and J. A. Orcutt (1992), Tomographic image of the axial-low velocity zone at 12°50′N on the East Pacific Rise, *J. Geophys. Res.*, *97*, 9243–9264.

Carlson, R. L., and G. S. Raskin (1984), Density of the ocean crust, *Nature*, *311*, 555–558.

Carton, H., S. M. Carbotte, J. C. Mutter, J. P. Canales, M. R. Nedimović, O. Aghaei, M. Marjanovic, and K. Newman (2010), Three-dimensional seismic reflection images of axial melt lens and seismic Layer 2A between 9 degree 42′N and 9 degree 57′N on the East Pacific Rise, Abstract OS21C-1514 presented at the 2010 Fall Meeting, AGU, San Francisco, Calif., 13–17 Dec.

Casey, J. F., and J. A. Karson (1981), Magma chamber profiles from the Bay of Islands ophiolite complex, *Nature*, *292*, 295–301.

Chapman, C. H., and J. A. Orcutt (1985), The computation of body wave synthetic seismograms in laterally homogeneous media, *Rev. Geophys.*, *23*(2), 105–163.

Christeson, G. L., W. S. D. Wilcock, and G. M. Purdy (1994), The shallow attenuation structure of the fast-spreading East Pacific Rise near 9°30′N, *Geophys. Res. Lett.*, *21*(5), 321–324.

Christeson, G. L., G. M. Kent, G. M. Purdy, and R. S. Detrick (1996), Extrusive thickness variability at the East Pacific Rise, 9°–10°N: Constraints from seismic techniques, *J. Geophys. Res.*, *101*, 2859–2873.

Christeson, G. L., P. R. Shaw, and J. D. Garmany (1997), Shear and compressional wave structure of the East Pacific Rise, 9°–10°N, *J. Geophys. Res.*, *102*, 7821–7835.

Collier, J. S., and S. C. Singh (1997), Detailed structure of the top of the melt body beneath the East Pacific Rise at 9°40′N from waveform inversion of seismic reflection data, *J. Geophys. Res.*, *102*(B9), 20,287–20,304.

Collier, J. S., and S. C. Singh (1998), A seismic inversion study of the axial magma chamber reflector beneath the East Pacific Rise near 10°N, in *Modern Ocean Floor Processes and the Geological Record*, edited by R. A. Mills and K. Harrison, pp. 17–28, Geological Society, London.

Collier, J. S., and M. C. Sinha (1990), Seismic images of a magma chamber beneath the Lau Basin back-arc spreading center, *Nature*, *346*, 646–648.

Detrick, R. S. (1991), Ridge crest magma chambers: A review of results from marine seismic experiments at the East Pacific Rise, in *Ophiolite Genesis and Evolution of the Oceanic Lithosphere*, edited by T. J. Peters, A. Nicolas, and R. G. Coleman, pp. 7–20, Kluwer Academic Publishers, Dordrecht.

Detrick, R. S., P. Buhl, E. E. Vera, J. C. Mutter, J. A. Orcutt, J. A. Madsen, and T. M. Brocher (1987), Multi-channel seismic imaging of a crustal magma chamber along the East Pacific Rise, *Nature*, *326*, 35–41.

Detrick, R. S., A. J. Harding, G. M. Kent, J. A. Orcutt, J. C. Mutter, and P. Buhl (1993), Seismic structure of the Southern East Pacific Rise, *Science*, *259*, 499–503.

Dunn, R. A., and D. R. Toomey (1997), Seismological evidence for the three-dimensional melt migration beneath the East Pacific Rise, *Nature*, *388*, 259–262.

Dunn, R. A., D. R. Toomey, and S. C. Solomon (2000), Three-dimensional seismic structure and physical properties of the crust and shallow mantle beneath the East Pacific Rise at 9° 30′N, *J. Geophys. Res.*, *105*, 23,537–23,555.

Fontaine, F. J., J.-A. Olive, M. Cannat, J. Escartín, and T. Perol (2011), Hydrothermally-induced melt lens cooling and segmentation along the axis of fast- and intermediate-spreading centers, *Geophys. Res. Lett.*, *38*, L14307, doi:10.1029/2011GL047798.

Fornari, D. J., et al. (2012), The East Pacific Rise Beween 9°N and 10°N: Twenty-five eyars of integrated, multidisciplinary oceanic spreading center studies, *Oceanography*, *25*(1), 18–43.

Fundis, A., S. A. Soule, D. Fornari, and M. R. Perfit (2010), Paving the seafloor: Volcanic emplacement processes during the 2005–2006 eruptions at the fast spreading East Pacific Rise, 9°50′N, *Geochem. Geophys. Geosyst.*, *11*, Q08024, doi:10.1029/2010GC003058.

Gilbert, L. A., and H. P. Johnson (1999), Direct measurement of oceanic crustal density at the northern Juan de Fuca Ridge, *Geophys. Res. Lett.*, *26*(24), 3633–3636.

Goss, A. R., M. R. Perfit, W. I. Ridley, K. H. Rubin, G. D. Kamenov, S. A. Soule, A. Fundis, and D. Fornari (2010), Geochemistry of lavas from the 2005–2006 eruption at the East Pacific Rise, 9°46′N–9°56′N: Implications for ridge crest plumbing and decadal changes in magma chamber compositions, *Geochem. Geophys. Geosyst.*, *11*, Q05T09, doi:10.1029/2009GC002977.

Greenbaum, D. (1972), Magmatic processes at ocean ridges: Evidence from the Troodos Massif, Cyprus, *Nat. Phys. Sci.*, *238*, 18–21.

Gudmundsson, A. (1995), The geometry and growth of dykes, in *Physics and Chemistry of Dykes*, edited by G. Baer and A. Heimann, pp. 23–34, Taylor and Francis, Rotterdam, Netherlands.

Han, S., S. M. Carbotte, H. Carton, J. C. Mutter, O. Aghaei, M. R. Nedimović, and J. P. Canales (2014), Architecture of off-axis magma bodies at EPR 9°37–40′N and implications for oceanic crustal accretion, *Earth Planet. Sci. Lett.*, *390*, 31–44.

Harding, A. J. (1985), Slowness-time mapping of near offset seismic reflection data, *Geophys. J. R. Astron. Soc.*, *80*, 463–492.

Harding, A. J., J. A. Orcutt, M. E. Kappus, E. E. Vera, J. C. Mutter, P. Buhl, R. S. Detrick, and T. M. Brocher (1989), The structure of young oceanic crust at 13°N on the East Pacific Rise from expanding spread profiles, *J. Geophys. Res.*, *94*, 12,163–12,196.

Harding, A. J., G. M. Kent, and J. A. Orcutt (1993), A multichannel seismic investigation of upper crustal structure at 9°N on the East Pacific Rise: Implications for crustal accretion, *J. Geophys. Res.*, *98*, 13,925–13,944.

Harper, G. D. (1984), The Josephine ophiolite, northwestern California, *Geol. Soc. Am. Bull.*, *95*, 1009–1026.

Hashin, Z., and S. Shtrikman (1963), A variational approach to the theory of the elastic behaviour of multiphase materials, *J. Mech. Phys. Solids*, *11*(2), 127–140.

Haymon, R. M., D. J. Fornari, M. H. Edwards, S. M. Carbotte, D. J. Wright, and K. C. Macdonald (1991), Hydrothermal vent distribution along the East Pacific Rise crest (9°09′–54′N) and its relationship to magmatic and tectonic processes on fast-spreading mid-ocean ridges, *Earth Planet. Sci. Lett.*, *104*, 513–534.

Haymon, R. M., et al. (1993), Volcanic eruption of the mid-ocean ridge along the East Pacific Rise crest at 9°45–52′N: Direct submersible observations of seafloor phenomena associated with an eruption event in April, 1991, *Earth Planet. Sci. Lett.*, *119*, 85–101.

Herron, T. J., W. J. Ludwig, P. L. Stoffa, T. K. Kan, and P. Buhl (1978), Structure of the East Pacific Rise crest from multichannel seismic reflection data, *J. Geophys. Res.*, *83*, 798–804.

Herron, T. J., P. L. Stoffa, and P. Buhl (1980), Magma chamber and mantle reflections - East Pacific Rise, *Geophys. Res. Lett.*, *7*, 989–992.

Hooft, E., and R. S. Detrick (1993), The role of density in the accumulation of basaltic melts at mid-ocean ridges, *Geophys. Res. Lett.*, *20*(6), 423–426.

Hussenoeder, S. A., J. A. Collins, G. M. Kent, R. S. Detrick, and the TERA Group (1996), Seismic analysis of the axial magma chamber reflector along the southern East Pacific Rise from conventional reflection profiling, *J. Geophys. Res.*, *101*, 22,087–22,105.

Hyndman, R. D., and M. J. Drury (1976), The physical properties of oceanic basement rocks from deep drilling on the Mid-Atlantic Ridge, *J. Geophys. Res.*, *81*(23), 4042–4052.

Kampfmann, W., and H. Berkhemer (1985), High temperature experiments on the elastic and anelastic behaviour of magmatic rocks, *Phys. Earth Planet. Inter.*, *40*(3), 223–247.

Kennett, B. L. N., and N. J. Kerry (1979), Seismic waves in a stratified half-space, *Geophys. J. R. Astron. Soc.*, *57*, 557–583.

Kent, G. M., A. J. Harding, and J. A. Orcutt (1990), Evidence for a smaller magma chamber beneath the East Pacific Rise at 9°30′N, *Nature*, *344*, 650–653.

Kent, G. M., A. J. Harding, and J. A. Orcutt (1993a), Distribution of magma beneath the East Pacific Rise near the 9°03′N overlapping spreading center from forward modeling of common depth point data, *J. Geophys. Res.*, *98*, 13,971–13,995.

Kent, G. M., A. J. Harding, and J. A. Orcutt (1993b), Distribution of magma beneath the East Pacific Rise between the Clipperton transform and the 9°17′N deval from forward modeling of common depth point data, *J. Geophys. Res.*, *98*, 13,945–13,969.

Kidd, R. G. W. (1977), A model for the process of formation of the upper oceanic crust, *Geophys. J. R. Astron. Soc.*, *50*, 149–183.

Korenaga, J., W. S. Holbrook, S. C. Singh, and T. A. Minshull (1997), Natural gas hydrates on the southeast U.S. margin: Constraints from full waveform and travel time inversions of wide-angle seismic data, *J. Geophys. Res.*, *102*(B7), 15,345–15,365.

Kormendi, F., and M. Dietrich (1991), Nonlinear waveform inversion of plane-wave seismograms in stratified elastic media, *Geophysics*, *56*(5), 664–674.

Livermore, R., A. Cunningham, L. Vanneste, and R. Larter (1997), Subduction influence on magma supply at the East Scotia Ridge, *Earth Planet. Sci. Lett.*, *150*, 261–275.

Lowenthal, D., L. Lu, R. Robertson, and J. Sherwood (1976), The wave equation applied to migration, *Geophys. Prospect.*, *24*, 380–399.

Macdonald, K. C., and P. J. Fox (1988), The axial summit graben and cross-sectional shape of the East Pacific Rise as indicators of axial magma chambers and recent volcanic eruptions, *Earth Planet. Sci. Lett.*, *88*, 119–131.

Macdonald, K. C., and J.-C. Sempéré (1984), East Pacific Rise from Siqueiros to Orozco fracture zones: Along-strike continuity of axial neovolcanic zone and structure and evolution of overlapping spreading centers, *J. Geophys. Res.*, *89*, 6049–6069.

MacLeod, C. J., and G. Yaouancq (2000), A fossil melt lens in the Oman ophiolite: Implications for magma chamber processes at fast spreading ridges, *Earth Planet. Sci. Lett.*, *176*, 357–373.

Mainprice, D. (1997), Modelling the anisotropic seismic properties of partially molten rocks found at mid-ocean ridges, *Tectonophysics*, *279*, 161–179.

Mavko, G. M. (1980), Velocity and attenuation in partially molten rocks, *J. Geophys. Res.*, *85*(B10), 5173–5189.

Minshull, T. A., S. C. Singh, and G. K. Westbrook (1994), Seismic velocity structure at a gas hydrate reflector, offshore western Columbia, from full waveform inversion, *J. Geophys. Res.*, *99*(B3), 4715–4734.

Mutter, J. C., G. A. Barth, P. Buhl, R. S. Detrick, J. A. Orcutt, and A. J. Harding (1988), Magma distribution across ridge-axis discontinuities on the East Pacific Rise from multichannel seismic images, *Nature*, *336*, 156–158.

Mutter, J. C., S. M. Carbotte, J. P. Canales, and M. R. Nedimović (2008), MGL0812 Cruise Report: A Three Dimensional MCS Investigation of the Magmatic-Hydrothermal System at the East Pacific Rise 9°50′N*Rep.*, 63 pp.

Mutter, J. C., S. Carbotte, M. R. Nedimović, J. P. Canales, and H. Carton (2009), Seismic imaging in three dimensions on the East Pacific Rise, *Eos Trans. AGU*, *90*(42), 374–375.

Nedimović, M. R., and G. F. West (2003), Crooked-line 2D seismic reflection imaging in crystalline terrains; Part 1, Data processing, *Geophysics*, *68*(1), 274–285.

Nicolas, A., and F. Boudier (2011), Structure and dynamics of ridge axial melt lenses in the Oman ophiolite, *J. Geophys. Res.*, *116*, B03103, doi:10.1029/2010JB007934.

Nicolas, A., F. Boudier, and G. Ceuleneer (1988), Mantle flow and magma chambers at mid-ocean ridges: Evidence from the Oman ophiolite, *Mar. Geophys. Res.*, *9*, 293–310.

Nicolas, A., C. Freydier, M. Godard, and A. Vauchez (1993), Magma chambers at oceanic ridges: How large?, *Geology*, *21*, 53–56.

Nicolas, A., F. Boudier, J. Koepke, L. France, B. Ildefonse, and C. Mevel (2008), Root zone of the sheeted dike complex in the Oman ophiolite, *Geochem. Geophys. Geosyst.*, *9*, Q05001, doi:10.1029/2007GC001918.

Nicolas, A., F. Boudier, and L. France (2009), Subsidence in magma chamber and the development of magmatic foliation in Oman ophiolite gabbros, *Earth Planet. Sci. Lett.*, *284*, 76–87.
Oliver, G. J. H., and R. R. McAlpine (1998), Occurrence of a sheeted dike dolerite dyke complex in the Ballantrae ophiolite, Scotland, *Geol. Mag.*, *135*, 509–517.
Pallister, J. S., and C. Hopson (1981), Samail Ophiolite plutonic suite: Field relations, phase variation, cryptic variation and layering, and a model of a spreading ridge magma chamber, *J. Geophys. Res.*, *86*(B4), 2593–2644.
Perfit, M. R., and W. W. Chadwick (1998), Magmatism at mid-ocean ridges: Constraints from volcanological and geochemical investigations, in *Faulting and Magmatism at Mid-Ocean Ridges*, edited by W. R. Buck et al., pp. 59–115, AGU, Washington, D. C.
Rosencrantz, E. (1983), The structure of sheeted dikes and associated rocks in North Arm massif, Bay of Islands ophiolite complex, and the intrusive process at oceanic spreading centers, *Can. J. Earth Sci.*, *20*, 787–801.
Rubin, K. H., J. D. Macdougall, and M. R. Perfit (1994), 210P0-210Pb dating of recent volcanic eruptions on the sea floor, *Nature*, *368*, 841–844.
Ryan, W. B. F., et al. (2009), Global multi-resolution topography synthesis, *Geochem. Geophys. Geosyst.*, *10*, Q03014, doi:10.1029/2008GC002332.
Scheirer, D. S., and K. C. Macdonald (1993), Variation in cross-sectional area of the axial ridge along the East Pacific Rise: Evidence for the magmatic budget of a fast spreading center, *J. Geophys. Res.*, *98*, 7871–7885.
Singh, S. C., G. M. Kent, J. S. Collier, A. J. Harding, and J. A. Orcutt (1998), Melt to mush variations in crustal magma properties along the ridge crest at the southern East Pacific Rise, *Nature*, *394*, 874–878.
Singh, S. C., J. S. Collier, A. J. Harding, G. M. Kent, and J. A. Orcutt (1999), Seismic evidence for a hydrothermal layer above the solid roof of the axial magma chamber at the southern East Pacific Rise, *Geology*, *27*(3), 219–222.
Singh, S. C., et al. (2006), Seismic reflection images of the Moho underlying melt sills at the East Pacific Rise, *Nature*, *442*, doi:10.1038/nature04939.
Sinton, J. M., and R. S. Detrick (1992), Mid-ocean ridge magma chambers, *J. Geophys. Res.*, *97*, 197–216.
Soule, S. A. (2012), Extent of new lava flow and Axial Summit Trough (AST) following 2005–06 eruption(s) at East Pacific Rise (EPR) 9°50′N, Integrated Earth Data Applications (IEDA), doi:10.1594/IEDA/100016.
Soule, S. A., D. J. Fornari, M. R. Perfit, and K. H. Rubin (2007), New insights into mid-ocean ridge volcanic processes from the 2005–2006 eruption of the East Pacific Rise, 9°46′N–9°56′N, *Geology*, *35*(12), 1079–1082.
Soule, S. A., J. Escartín, and D. Fornari (2009), A record of eruption and intrusion at a fast spreading ridge axis: Axial summit trough of the East Pacific Rise 9-10°N, *Geochem. Geophys. Geosyst.*, *10*, Q10T07, doi:10.1029/2008GC002354.
Taylor, M. A. J., and S. C. Singh (2002), Compositions and microstructure of magma bodies from effective medium theory, *Geophys. J. Int.*, *149*, 15–21.
Toksöz, M. N., R.-S. Wu, and D. P. Schmitt (1987), Physical mechanisms contributing to seismic attenuation in the crust, in *Strong Ground Motion Seismology*, NATO ASI Series, vol. 204, edited by M. Erdik and M. N. Töksoz, pp. 225–247, Springer, Netherlands.
Tolstoy, M., et al. (2006), A sea-floor spreading event captured by seismometers, *Science*, *314*, 1920–1922.
Tompkins, M. J., and N. I. Christensen (2001), Ultrasonic P- and S-wave attenuation in oceanic basalt, *Geophys. J. Int.*, *145*, 172–186.
Toomey, D. R., G. M. Purdy, S. C. Solomon, and W. S. D. Wilcock (1990), The three-dimensional seismic velocity structure of the East Pacific Rise near latitude 9°30′N, *Nature*, *347*, 639–645.
Toomey, D. R., S. C. Solomon, and G. M. Purdy (1994), Tomographic imaging of the shallow crustal structure of the East Pacific Rise at 9°30′N, *J. Geophys. Res.*, *99*, 24,135–24,157.
Toomey, D. R., D. Jousselin, R. A. Dunn, W. S. D. Wilcock, and R. S. Detrick (2007), Skew of mantle upwelling beneath the East Pacific Rise governs segmentation, *Nature*, *446*, 409–414.
Tryggvason, E. (1994), Surface deformation at the Krafla Volcano, North Iceland, 198201992, *Bull. Volcanol.*, *56*(2), 98–107.
Umino, S., S. Miyashita, F. Hotta, and Y. Adachi (2003), Along-strike variation of the sheeted dike complex in the Oman ophioliteL Insights into subaxial ridge segment structures and the magma plumbing system, *Geochem. Geophys. Geosyst.*, *4*(9), 8618, doi:10.1029/2001GC000233.
Vera, E. E., J. C. Mutter, P. Buhl, J. A. Orcutt, A. J. Harding, M. E. Kappus, R. S. Detrick, and T. M. Brocher (1990), The structure of 0- to 0.2-m.y.-old oceanic crust at 9°N on the East Pacific Rise from expanded spread profiles, *J. Geophys. Res.*, *95*, 15,529–15,556.
Wanless, V. D., and A. M. Shaw (2012), Lower crustal crystallization and melt evolution at mid-ocean ridges, *Nat. Geosci.*, *5*, 651–655.
Wepfer, W. W., and N. I. Christensen (1991), Q structure of the oceanic crust, *Mar. Geophys. Res.*, *13*, 227–237.
White, S. M., R. M. Haymon, D. J. Fornari, M. R. Perfit, and K. C. Macdonald (2002), Correlation between volcanic and tectonic segmentation of fast-spreading ridges: Evidence from volcanic structures and lava flow morphology on the East Pacific Rise at 9°–10°N, *J. Geophys. Res.*, *107*(B8), 2173, doi:10.1029/2001JB000571.
White, S. M., R. M. Haymon, and S. Carbotte (2006), A new view of ridge segmentation and near-axis volcanism at the East Pacific Rise, 8°–12°N, from EM300 multibeam bathymetry, *Geochem. Geophys. Geosyst.*, *7*, Q12O05, doi:10.1029/2006GC001407.
Wilcock, W. S. D., S. C. Solomon, G. M. Purdy, and D. R. Toomey (1992), The seismic attenuation structure of a fast-spreading mid-ocean ridge, *Science*, *258*, 1470–1474.
Wilcock, W. S. D., S. C. Solomon, G. M. Purdy, and D. R. Toomey (1995), Seismic attenuation structure of the East Pacific Rise near 9°30′N, *J. Geophys. Res.*, *100*, 24,147–24,165.
Xu, M. (2012), Advanced Geophysical Studies of Accretion of Oceanic Lithosphere in Mid-Ocean Ridges Characterized by Contrasting Tectono-Magmatic Settings, PhD thesis, 253 pp., Massachusetts Institute of Technology/Woods Hole Oceanographic Institution Joint Program in Oceanography.
Yilmaz, Ö. (1987), *Seismic Data Processing*, 526 pp., Society of Exploration Geophysicists, Tulsa, Okla.